General Synthetic Strategy to Ordered Mesoporous Carbon Catalysts with Single-Atom Metal Sites for Electrochemical CO₂ Reduction

Zhicheng Luo⁺, Zhouyang Yin⁺, Jiaqi Yu, Yu Yan, Bing Hu, Renfeng Nie, Anna F. Kolln, Xun Wu, Ranjan K Behera, Minda Chen, Lin Zhou, Fudong Liu, Bin Wang, Wenyu Huang,* Sen Zhang,* Long Qi*

Dr. Z. Luo, Dr. L. Zhou, Dr. L. Qi U.S. DOE Ames Laboratory Iowa State University Ames, Iowa 50011, United States

E-mail: <u>lqi@iastate.edu</u>

Dr. Z. Yin, Prof. S. Zhang Department of Chemistry University of Virginia Charlottesville, Virginia 22904, United States E-mail: sz3t@virginia.edu

Jiaqi Yu, Renfeng Nie, Anna F. Kolln, Xun Wu, Ranjan K Behera, Minda Chen, Prof. W. Huang
Department of Chemistry
Iowa State University
Ames, Iowa 50011, United States
Email: whuang@iastate.edu

Y. Yan, Prof. B. Wang School of chemical, Biological and Materials Engineering University of Oklahoma Norman, OK 73019, United States

Dr. B. Hu Institute for Catalysis Hokkaido University Hokkaido 001-0021, Japan

Orlando, FL 32816, United States

Prof. F. Liu
Department of Civil, Environmental, and Construction Engineering
Catalysis Cluster for Renewable Energy and Chemical Transformations (REACT)
NanoScience Technology Center (NSTC)
University of Central Florida

Keywords: electrochemical CO₂ reduction, general synthesis, ordered mesoporous structure, single-atom catalysts, DFT calculation

Abstract: Electrochemical carbon dioxide reduction reaction (CO₂RR) is a transformative technology to reduce carbon footprint of modern society. Single-site catalysts have been demonstrated as promising catalysts for CO₂RR, but general synthetic methods for catalysts with high surface area and tunable single-site metal composition still need to be developed to unambiguously investigate the structure-activity relationship crossing various metal sites. Here, we report a generalized coordination-condensation strategy to prepare single-atom metal sites on ordered mesoporous carbon (OMC) with high surface areas (average 800 m² g⁻¹). This method is applicable to a broad range of metal sites (Fe, Co, Ni, Cu, Pt, Pd, Ru, and Rh) with loadings up to 4 wt%. In particular, the CO₂RR to carbon monoxide (CO) Faradaic efficiency (FE) with Ni single-site OMC catalyst reaches 95%. This high FE maintains even under large current density (>140 mA/cm²) and in a long-term study (14 hours), which is suited to urgently needed large-scale applications. Theoretical calculations suggest that the enhanced activity on single-atom Ni sites results from balanced binding energies between key intermediates, COOH and CO, for CO₂RR, as mediated by the coordination sphere.

1. Introduction

The conversion and utilization of CO₂ is highly demanded on the verge of technology revolution towards carbon neutrality and cyclic economy.^[1] Catalytic systems that would transform CO₂ into commodity chemicals can not only mitigate CO₂ footprint but also create new streams of feedstock supply, which may reshape the landscape of chemical manufacturing. Electrocatalytic CO₂ reduction reaction (CO₂RR) is an emerging technology that meets these requirements and has attracted enormous attention.^[2] The scaled application of CO₂RR requires catalytic systems to be energy-efficient and readily scalable, using earth-abundant elements. Various catalytic materials have been explored, among which single-atom catalysts demonstrated great potentials for selective CO₂RR to CO product.^[3] Ni single-atom catalyst is the most promising one and has obtained enormous interest since 2016.^[4] Single-atom Ni sites

anchored on various carbon supports, including graphene,^[4] graphene oxide,^[5] carbon black,^[6] and carbonfiber,^[7] were reported to be highly selective for CO production (FE>80%). Single-atom catalysts are more appealing than other catalytic materials with larger physical dimensions (e.g., bulk or nanoscale metallic materials) which often lead to mixed products with poor selectivities. Moreover, the resulting CO can be subsequently converted to longer-chain hydrocarbons and oxygenates via well-established Fischer-Tropch^[8] or tandem electrochemical conversion.^[9] Other single-atom catalysts studied for CO₂RR include Fe,^[10] Zn,^[11] Co,^[12] and Cu.^[13]

Despite these advances, there are significant synthetic challenges in preparing single-atom catalysts for the scaled application of CO₂RR. First, the desirable catalytic materials need to present largely accessible surface area and effective exposure of single-atom sites of high loading, rendering the electrochemical process amenable for high current-density operation. Second, the accurate understanding of structure-property relationship requires the generalized anchoring of single-atom sites with uniform short- and long-range structures crossing a broad range of metal compositions. Several general synthetic methods have been proposed, and the thermodynamics of different metal sites have been explored.^[14] For instance, *in situ* anchoring of metal ions during carbon synthesis via pyrolysis can be achieved with the assistance of different nitrogen sources such as bipyridine, phenylenediamine, or urea.^[14b,15] Also, *ex situ* grafting of metal sites was investigated on pre-synthesized N-doped graphene.^[16] However, most of these catalysts are of relatively low surface area and/or low metal loading ^[6], limiting the amount of surface-exposed active sites and mass transfer.

Here, we report a generalized synthetic strategy to prepare nitrogen-doped ordered mesoporous carbon embedded with controllable single-atom metal site compositions (Fe, Co, Ni, Cu, Pt, Pd, Ru, and Rh). This approach takes advantage of the strong coordination of metal cations with ethylene diamine (the nitrogen source), allowing metal sites to remain isolated prior to pyrolysis. The templated synthetic method leads to the formation of ordered mesoporous architecture that

enables the efficient exposure of metal sites and improved mass transfer properties. The uniform local structure of the tunable metal sites makes it possible to rapidly benchmark their catalytic performances in CO₂RR. Benefiting from the metal-nitrogen bonding and ordered mesoporous structure, the selectivity and stability of the single-site catalysts during CO₂RR are tremendously improved. Specifically, the CO selectivity with single-atom Ni site catalyst reaches 95% under moderate overpotentials and neutral conditions. Density functional theory (DFT) calculations show that the binding of COOH and CO is balanced on single-atom Ni, and the reaction kinetics for the first protonation to CO₂ is facilitated by reducing the nitrogen coordination to the metal center.

2. Results and Discussion

2.1. Synthesis and Characterization

To synthesize the catalysts, ethylenediamine is used as a strong chelating ligand to stabilize both base and precious metal atoms. [17] Moreover, ethylenediamine acts an ideal N source for the carbon materials and its high N/C ratio in ethylenediamine ensures the high N content in the final catalyst even after pyrolysis, which is successfully demonstrated in our previous work in the synthesis of nitrogen assembly carbons (NACs). [18] We use the Ni-NAC as an example to demonstrate this general coordination-condensation strategy. Ni^{II} acetylacetonate was firstly dispersed in the ethylenediamine, followed by the slow addition of carbon tetrachloride. A mesoporous silica template (SBA-15) was then added for the further condensation reaction to proceed in the mesopores. After 16 h at 90 °C, the solid-liquid mixture completely solidifies into a brown mixture. The obtained polymer was then carbonized at 800 °C under Ar while the Ni^{II} ions, together with their coordination spheres, were integrated into the graphitic domain of the NAC support as isolated metal sites. After removing the silica template by etching, the Ni-NAC catalyst can thus be isolated. More importantly, this general strategy can be readily

applied to synthesize other metal(M)-NACs (including Fe^{III} , Co^{II} , Cu^{II} , Ru^{III} , Rh^{II} , Pd^{II} , and Pt^{II}) from the corresponding acetylacetonates.

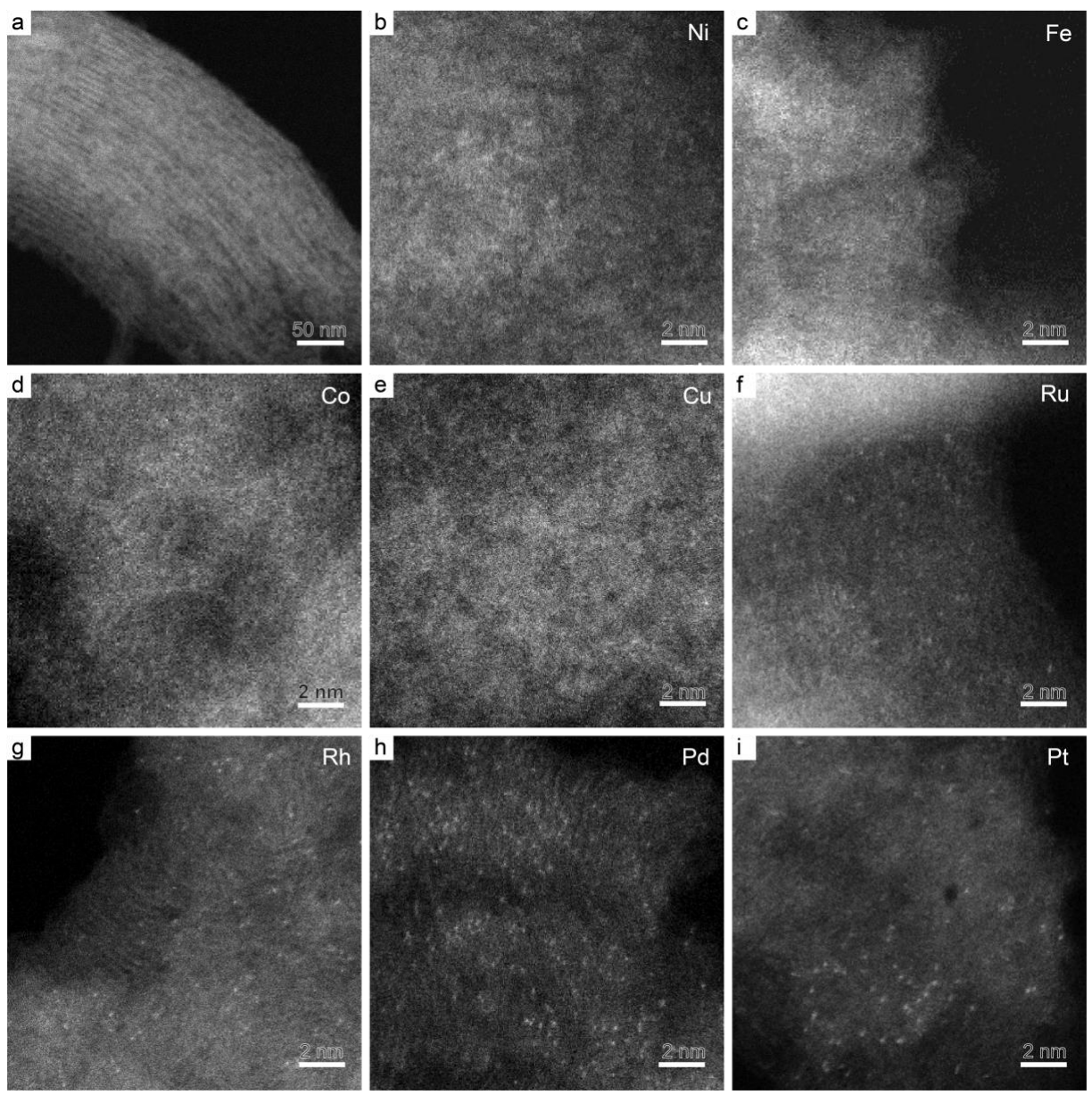


Figure 1. HAADF STEM images of various metal single-atom catalysts. (a) low magnification image of Ni-NAC. Atomic resolution images of (b) Ni-NAC, (c) Fe-NAC, (d) Co-NAC, (e) Cu-NAC, (f) Ru-NAC, (g) Rh-NAC, (h) Pd-NAC, and (i) Pt-NAC.

All M-NACs exhibit the rod-shaped morphology (Figures 1a and S1) with aligned and well-ordered mesopores and high surface areas, owing to the use of the ordered mesoporous silica template. N₂ physisorption results show type IV isotherm for all samples, characteristic of ordered mesoporous materials. The surface areas are calculated to be 720-930 m² g⁻¹, and pore diameters are 3.4-5.5 nm (Table S1). The high monodispersity of the mesopores, long-range

ordering, and high surface areas are unique features of these M-NACs, when compared to other reported catalysts for CO₂RR.^[19]

Fig 1a is a high-angle-annular-dark-field (HAADF) scanning transmission electron microscopy (STEM) image that shows the ordered mesoporous structure of Ni-NAC at low magnification. Single metallic atoms are directly revealed as bright dots dispersed on the NAC support without any noticeable presence of nanoparticles in aberration-corrected STEM images (Figures 1b-1i). The powder X-ray diffraction patterns of M-NACs (Figure S2) show no signals of metal nanoparticles. The two broad diffraction peaks, centered at *ca.* 25° and 44°, correspond to the (002) and (100) planes of the NAC matrix, agreeing with STEM images (Figures 1b-1i). Elemental analysis shows the metal loading for base metal-NACs to be Fe (0.7 wt%), Ni (1.7 wt%), Co (1.6 wt%), and Cu (4.2 wt%), respectively. X-ray photoelectron spectra (XPS) of the M-NAC catalysts shows only signals for carbon, nitrogen, oxygen, and correponsponding metals (Figure S2). The Fe2*p*, Co2*p*, Ni2*p*, Cu2*p*, Pd3*d*, and Pt4*f* XPS spectra for the M-NACs (Figure S4) show that the binding energies of these metals correspond to Fe^{III}, Co^{II}, Ni^{II}, Cu^{II}, Pd^{II}, and Pt^{II} species, respectively, for the corresponding catalysts, with the same oxidation state as the starting metal precursor.

XPS and CHN elemental analysis (Table S2) both demonstrate that the M-NACs are mainly composed of carbon (81.3-86.7 at%) and nitrogen (8.1-11.7 at%) with the C:N ratio at the range of 7.0 to 10.7, indicating the uniform distribution of nitrogen on the surface and bulk of the M-NACs. The N1s spectra (Figure S5 and Table S3) for the M-NACs could be deconvoluted into five peaks, corresponding to the pyridinic N, metal-N, pyrrolic N, graphitic N, and pyridinic N-oxide, respectively.^[20] These surface-rich N atoms provide additional binding sites to increase surface concentration of CO₂.^[21] The non-innocent surface of carbon support is populated with graphitic nitrogen assembly.^[22] These nitrogen assembly sites, composed of closely-spaced graphitic nitrogens rather than isolated ones,^[18] can modify the electronic density of the metal

centers and serve as co-catalyst in multi-step electric processes when multiple binding sites are demanded.

2.2. Structural Identification of the Active Sites

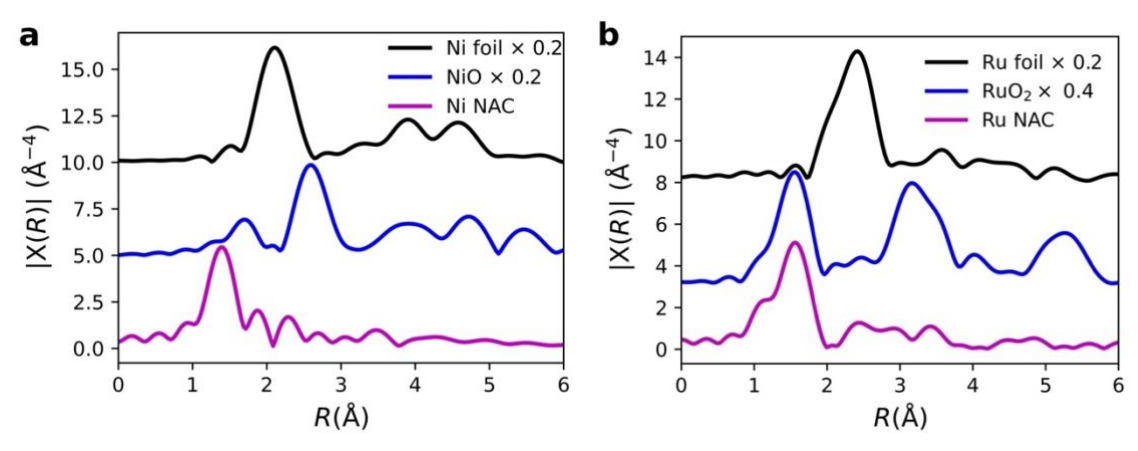


Figure 2. R-space plots of metal K-edge EXAFS of (a) Ni-NAC and (b) Ru-NAC in comparison with those of the corresponding metal foil and metal oxide reference standards after Fourier transform of k^3 -weighted $\chi(k)$ of the same k range.

Extended X-ray absorption fine structure (EXAFS) is a powerful tool for probing the coordination environment of metal atoms. The Fourier transform of the EXAFS oscillation gives peaks corresponding to various coordination shells around the metal center, which is the R-space plot as shown in Figures 2 and S6. For all M-NACs, only a single main peak before 2 Å can be observed in R-space plot, indicating the existence of only light scatters around the single-atom metal site, rather than metal-metal scattering path as in the corresponding metal foils or higher scattering path such as M-O-M in metal oxides. Quantitatively, the least-square peak fitting analysis of the EXAFS shows that all M-NACs have MX4 moiety with univariate or bivariate M-X bond length except Ru and Fe (Figures S7-S17). X can be C, N, or O, which are challenging to distinguish. For example, the EXAFS of Ni-NAC can be fitted with two Ni-N paths with bond lengths of (1.87 ± 0.01) and (2.05 ± 0.02) Å (Figure S9), which are very close to the Ni-N bond distance in molecular Ni^{II} phthalocyanine or porphyrin complex $(1.90 \text{ Å})^{[23]}$ and amine-coordinated Ni complex. [24] The use of three single scattering paths of Ni-N1, Ni-N2, and Ni-C can also give reasonable fitting results (Figure S10). Similarly, for Cu-NAC,

a good EXAFS fitting can be achieved by using either one path of Cu-N (Figure S11), or two paths of Cu-N (degeneracy is 3) and Cu-C (Figure S12). For Fe^{III}- and Ru^{III}-NAC, an additional M-X scattering path is included for accurate curve fittings (Figures S7 and S13). Considering the oxidation state of Ru or Fe is +3, the fifth coordination is likely to balance the charge at the Ru center with a mono-anionic ligand; therefore, the most likely extra path is hydroxide (OH⁻) in an axial geometry. It is important to note that our new synthetic method is likely to retain the oxidation state of the metal precursors, which is the key to synthesizing the desired catalysts on demand.

The X-ray absorption near edge structure (XANES) region can reflect the chemical state of the metal center and is sensitive to the 3-dimensional arrangement of scatters around. From the comparison of XANES spectra (Figure S18), the valence of Cu in Cu-NAC is very close to that of CuO, while Co, Ni, and Pt in M-NACs are in between that of metallic foil and highest valence oxide. Judging from the position and intensity of the main peak in the K-edge that stems from 1s to 4p transition, Fe-NAC has a valence state close to Fe₂O₃. [25] Similarly, the valence of Ru in Ru-NAC is a little lower than that of RuO2. These are in accordance with XPS analysis. For the Fe-, Co-, Ni-, and Cu-NACs' K-edge XANES spectra, the shoulder peak in the middle of the K-edge is ascribed to 1s-4p shakedown excitation, which is much weaker than that of a square planar species with D_{4h} symmetry, [26] indicating the distortion of or deviation from the planar structure. The XANES spectra of various MN_4C_x (Fe- and Ru-O₁N₄C_x) structures with bonding metrics according to EXAFS analysis were calculated using FEFF8 program and compared with the experimental data (Figures S19-26). The main features of experimental XANES can be well reproduced by non-planar or distorted planar MN₄ moieties. Notably, for Ni-NAC, Cu-NAC, and Pt-NAC, we found that a metal center of MN₃C₁ gives better simulations of the XANES features than MN₄ (Figures S21, S22, and S26). Besides, XANES simulation corroborates the existence of M-O bond at the metal center of Fe-NAC and Ru-NAC (Figures S19 and S23).

2.3. Electrocatalytic CO₂RR over M-NACs

The NAC support provides a highly versatile platform to accommodate different single atom metal sites, based on which we tested their electrocatalytic properties for CO₂RR. Base metals are more abundant than precious metals, so we began with Fe, Cu, Co, and Ni single atom catalysts. Before each test, we run cyclic voltammetry (CV) in both Ar-saturated and CO₂saturated KHCO₃ solutions. As shown in Figure S27, there are no metal redox peaks during CV scans in either Ar or CO₂, which is in line with our expectation that metal atoms are stabilized in the NACs and cannot be easily reduced or oxidized. From the CVs, the currents start to increase at about -0.6 V vs. reversible hydrogen electrode (RHE), suggesting CO₂RR and hydrogen evolution reaction (HER) happens at this potential. Thus, we choose -0.6 V to -1.4 V vs. RHE as our potential range. Fe-NAC single-atom catalyst generates either more CO (at -0.6 V) or more H_2 (< -0.8 V) (Figure 3a). The potential-dependent CO/ H_2 selectivity of Fe-NAC makes it a good candidate for syngas generation. Cu materials are known to be active for the production of high-value carbon products, such as ethylene and ethanol. [27] However, the Cu-NAC single-atom catalyst, as shown in Figure 3b, generates a mixture of CO and H₂. As the applied potential decreased from -0.6 V to -1.2 V vs. RHE, CO FE increased from 5.3% to 21.1%, and there were no other carbon products detected. The FE of CO generation with Co-NAC catalyst is similar to Cu-NAC catalyst, which reaches 21.3% at -0.6 V (Figure 3c) but starts to decrease with more negative potentials. Among all the base metal single-atom catalysts prepared, Ni-NAC is the most promising and generates 95% CO at -1.0 V (Figure 3d), with no liquid products observed (Figure S28). In addition, the CO FE with Ni-NAC remains high (> 85%) at a wide potential range from -0.8 V to -1.4 V. We also synthesized a metal-free catalyst calcined at 800 °C (NAC-800) as a control. As shown in Figure 3e, The CO selectivity of NAC-800 catalyst is clearly lower than Ni-NAC and Fe-NAC, suggesting that N-doped site itself is not the dominant reaction site for CO generation. Additionally, HER keeps increasing as the potential decreases, suggesting that NAC-800 could not work in high overpotential conditions.

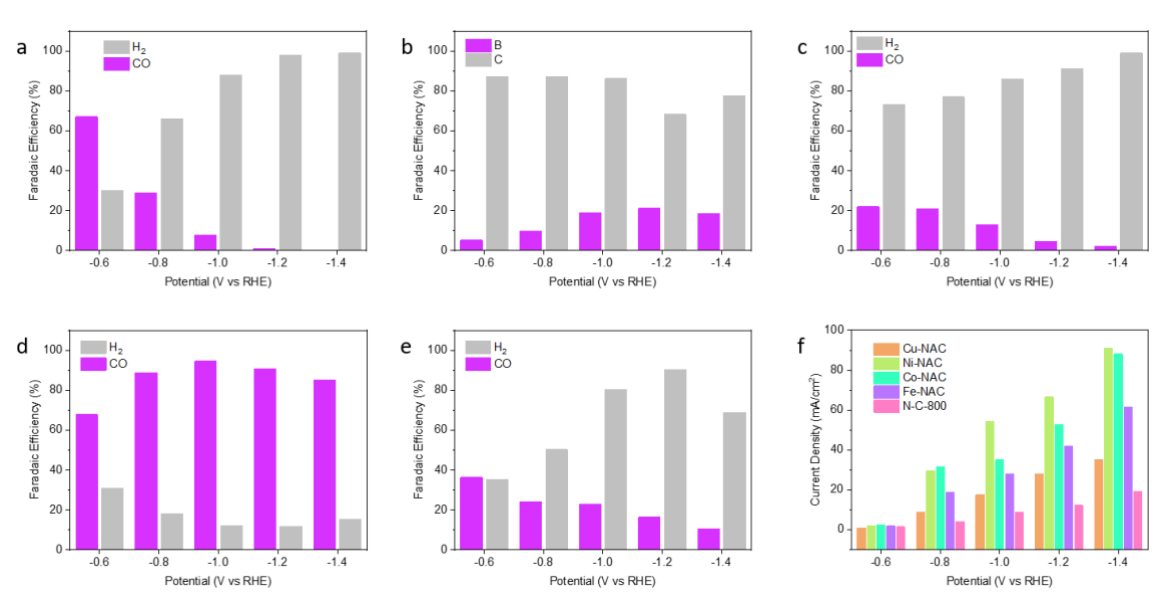


Figure 3. Products distribution of CO₂RR catalyzed by (a) Fe-NAC, (b) Cu-NAC, (c) Co-NAC, (d) Ni-NAC, and (e) NAC-800 catalyst at different reduction potentials. (f) Reduction current density of different catalysts at different reduction potentials.

The current densities of all these catalysts were carefully monitored. As shown in Figure 3f, Ni-NAC shows the highest current density at nearly every tested potential from -0.6 V to -1.4 V, while NAC-800 has the lowest current density. Specifically, with Ni-NAC as the catalyst for CO₂ reduction at -1.4 V, the CO FE is higher than 85%, and the current density reaches 91 mA/cm². The current density of Fe-NAC, Cu-NAC, and Co-NAC is lower than Ni-NAC but higher than NAC-800. However, the selectivity towards CO formation is much worse than Ni-NAC.

We then should study precious metal catalysts to provide a comprehensive comparison with base metal samples. However, HER is dominating under every potential with all the noble metal catalysts, and only Rh-NAC and Pd-NAC could generate moderate CO (< 10% for Rh-NAC and 25% for Pd-NAC) (Figure S29). The CV spectrum of Pt-NAC (Figure S27) also shows that the current starts to increase before -0.6 V, which is attributed to the HER.

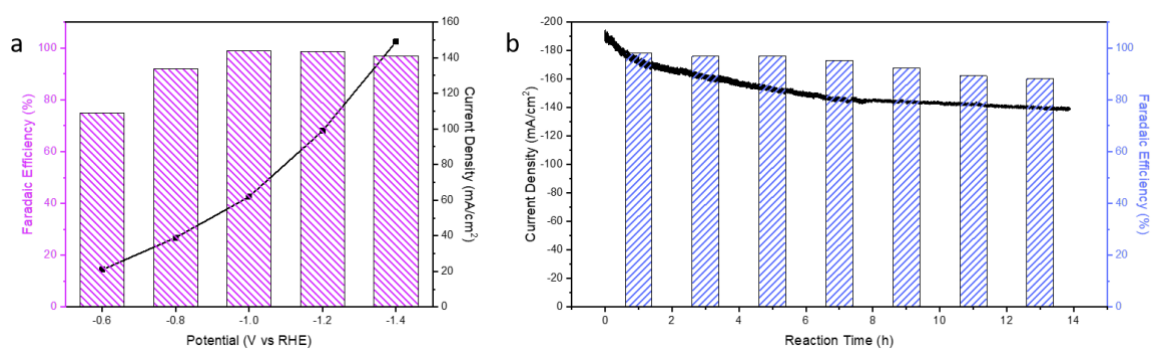


Figure 4. (a) CO FE and current density with Ni-NAC catalyst in flow cell at different potential. (b) CO FE and current density with Ni-NAC catalyst in flow cell for 14 hours.

The CO₂ reduction results in H-cell suggest that Ni-NAC is the best single-atom candidate for CO₂RR. To further enhance the CO₂RR activity of Ni-NAC, a gas-diffusion cell is applied. With gas-diffusion cell to further improve the CO₂ mass transfer, both current density and FE have improved, agreeing with our expectation. The CO FE starts from 75% at -0.6 V and keeps higher than 90% from -0.8 V to -1.4 V (Figure 4a). Compared with the current density in H-cell of less than 100 mA/cm², the current density with flow cell increases to 151 mA/cm². The Ni-NAC possesses not only high CO selectivity and current density but also high robustness during CO₂RR. To the best of our knowledge, our Ni-NAC catalyst is among the high-performance Ni single atom catalysts (Table S4). Electrolysis with Ni-NAC electrode is performed under -1.4 V in a flow cell for 14 hours. The current density drops slightly from 190 to 142 mA/cm² after 14 hours, and the CO FE remains around 90% (Figure 4b).

2.4. Theoretical Investigation

The CO₂RR activity on each CO-producing metal (Ni, Fe, Co, and Cu) was studied here with DFT calculations. Normally, CO₂ reduction toward CO requires two proton-electron transfers in a concerted mechanism. The first transfer of a combined proton and electron to CO₂ produces the COOH intermediates, which is consequently converted into an adsorbed CO through the second proton-electron transfer. Figure 5 reports the CO₂RR free energy profile through which the potential-limiting step can be identified. Formation of the COOH intermediate limits the rate on Ni and Cu on N₄-doped graphene (NiN₄ and CuN₄), in agreement with literature.^[28]

While on FeN₄ and CoN₄, the reduction of CO₂ is limited by CO desorption with an energy cost of 1.3 and 0.6 eV, respectively.

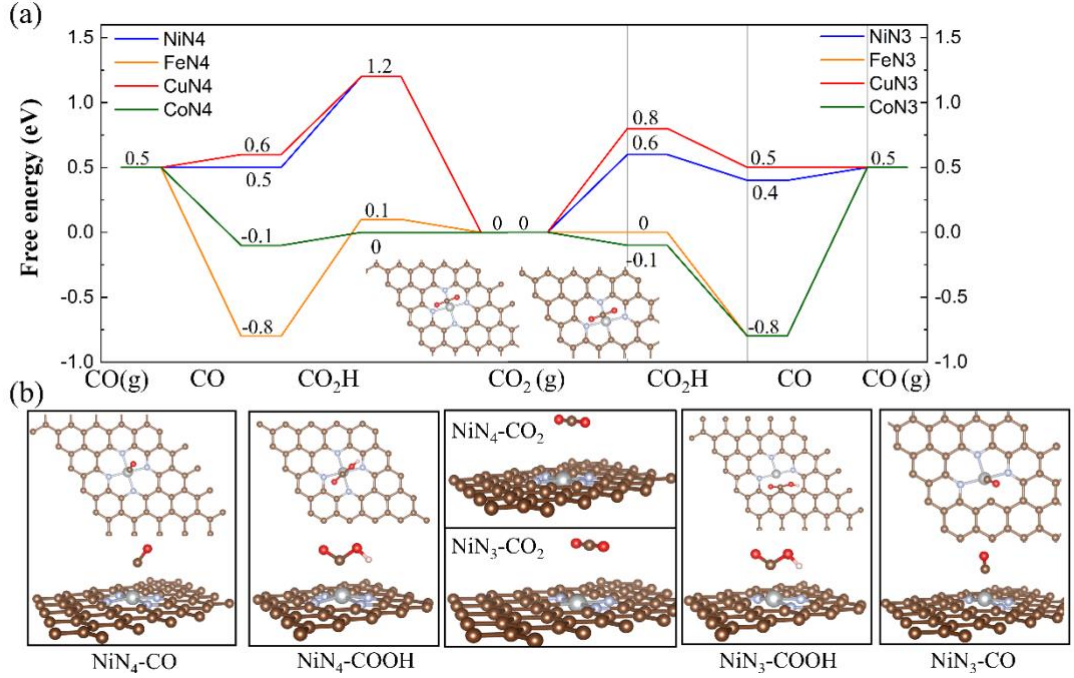


Figure 5. DFT-calculated CO₂RR profile on metal NAC. (a) CO₂RR Free energy diagram on base metals single atom on N-doped graphene. (b) The calculated structures for intermediate CO₂, COOH, and CO from the top and side point of view.

The activity is very sensitive to the local coordination of the single metal. Here we show the single metal atom could also bind with both carbon and nitrogen (N_xC_{4-x}) instead of four nitrogen neighbors. Since the characterization techniques such as EXAFS cannot distinguish neighboring carbon and nitrogen unambiguously, we investigate the CO₂RR performance of Ni single atom in a configuration of N₄, N₃C₁, N₂C₂, and N₁C₃, and find that when coordinating with more C atoms, the intermediate species, COOH and CO, bind stronger to the active site. The metal N₃C₁ structure has the highest activity with the lowest energy cost for the potential-limiting step (Figure S30). Furthermore, we show that, on NiN₃ and CuN₃, the COOH species could be further stabilized on the neighboring carbon rather than the metal, reducing the energy cost of first proton transfer to 0.8 and 0.9 eV on Ni and Cu, respectively. The carbon in the first coordination shell thus not only modifies the electronic property of the metal but also provides an additional site for the adsorption of reaction intermediates. CO desorption remains to limit

the reaction kinetics over FeN₃ and CoN₃ due to its strong adsorption. The possible MN₃C coordination structures of Ni and Cu are supported by the XANES simulation. Our calculations thus provide an explanation for the experimental observation that Ni single atoms are the most active among the tested base metals.

Results of HER calculations are also included in Figure S31 and S32. It shows Fe and Co in both N₄ and N₃ configurations can catalyze HER efficiently, which agrees with the product distribution in Figure 3. The HER activity over CuN₄ should be much lower, due to the weak adsorption of hydrogen, than it on CuN₃C; the dominant selectivity to H₂ over Cu samples in experiments indicates that the CuN₃C configuration is more likely in the experiments, in agreement with the XANES simulation. To unambiguously determine and correlate the Ni coordination structure with the catalytic activity and selectivity, calculations that include activation barriers, explicit solvent, electrode potential, and different spin states should be explored.

3. Conclusion

In summary, we introduce an innovative general method to prepare single-site catalysts of various metal elements supported on ordered mesoporous carbon. Examples have been demonstrated for metals including Fe, Co, Ni, Cu, Ru, Rh, Pd, and Pt. The strong coordination of metal cations with ethylene diamine enables a high loading of atomically dispersed metal embedded into the carbon support. Features of these M-NAC catalysts include the high metal loading, well ordered meso-structures, and high surface areas. These features permit superior activity, efficient mass transfer, and large current as CO₂RR catalyst. Among all the M-NAC catalysts, Ni-NAC shows the highest CO selectivity, which generates more than 95% CO at moderate potentials. Other base metal-NAC, such as Co-NAC, and Cu-NAC, produce a mixture of CO and H₂, which are great candidate catalysts for syngas generation. Unlike the non-noble metal-NAC, noble metal-NAC (Ru, Rh, Pd and Pt), have no electrochemical CO₂RR activity

but are potential HER catalysts. DFT calculations suggest rational design of the metal and its coordination environment is valuable for promoting the CO_2RR activity.

4. Experimental Section

Chemcials: Iron(III) acetylacetonate (≥99.5%, trace metal), cobalt(II) acetylacetonate (≥99%), nickel(II) acetylacetonate (95%), copper(II) acetylacetonate (≥99.9%, trace metal), ruthenium(III) acetylacetonate (97%), platinum(II) acetylacetonate (≥99.8%, trace metal), palladium(II) acetylacetonate (98%), carbon tetrachloride (≥99.9%), ethylenediamine (≥99.5%), tetraethyl orthosilicate (TEOS, 98%), and pluronic P123 (Mn~5,800) were purchased from Sigma-Aldrich. Hydrofluoric acid (TraceMetal grade), hydrochloric acid (TraceMetal grade), and nitric acid (TraceMetal grade) were purchased from Fisher Chemical. N-Methyl-2-pyrrolidone (NMP) were purchased from Fisher Scientific. Platinum wire (0.5 mm diameter, Premion®, 99.997%), Toray Carbon Paper (TGP-H-60) was from Alfa Aesar. Polyvinylidene fluoride (PVDF) was from MTI corporation. All chemicals were used as received.

Synthesis of SBA-15. 6 g Pluronic P123 was firstly dissolved in 180 mL 2M hydrochloric solution at 40 °C with the help of stirring (500 rpm) in a 500 mL sealed polypropylene bottle. After being dissolved, 12.75 g of TEOS was added, and the solution was kept stirring for 20 h. The composition of the achieved gel was: 1 TEOS: 0.017 P123: 5.68 HCl: 197 H₂O. After 20 h, the whole bottle was kept in oven at 100 °C for 24 h under static condition. The white precipitant was recovered by Büchner filtration, washed with ultrahigh purity water/methanol 1:1 volume ratio twice, and it was kept in the hood for three days for air dry. The obtained solid was heated to 550 °C under air at a heating rate of 2 °C min⁻¹ and calcined for 5 h.

Synthesis M-NACs. The corresponding metal acetylacetonate was firstly added into the solution of ethylenediamine (1.80 g) and carbon tetrachloride (4.00 g), followed by adding SBA-15 (0.80 g). *Caution: the metal precursor may catalyze the condensation of carbon tetrachloride and ethylenediamine with the release of HCl gas.* The mixture was then heated in an oil bath at 90 °C for 16 h for condensation before the oil bath temperature increased to 120 °C for 4 h to remove the uncondensed ethylenediamine and carbon tetrachloride. The obtained

powders were calcined under Ar flow, with temperature raised at a ramping rate of 3 °C min⁻¹ and further maintained at 800 °C for 2 h. The achieved black powder was then etched with 5 wt% HF solution to remove the SBA-15. The catalyst was recovered via centrifuge, washed with deionized water until the pH reached 7. The catalyst was further dried at 100 °C for future usage.

Characterization. Aberration corrected HAADF STEM imaging was performed using a probecorrected Thermo Fisher (FEI) Titan Themis. Powder X-ray diffraction (XRD) was carried out on a Bruker D8A25 diffractometer with Cu $K\alpha$ radiation ($\lambda = 1.54184$ Å). N₂ physisorption was performed using an auto-adsorption analyzer (Micromeritics, 3Flex) at -196 °C. Elementary analysis was conducted using a Perkin Elmer 2100 Series II CHN/S Analyzer. Inductively coupled plasma mass spectroscopy (ICP-MS) for metal loadings was performed using a Thermo Fisher Scientific X Series 2 spectrometer. X-ray photoelectron spectrometry (XPS) was recorded on a PerkinElmer PHI ESCA system with Physical Electronics (PHI). X-ray absorption spectroscopy (XAS) of the Ni, Cu, Ru, Pt-NAC catalysts were measured at Beamline 9-BM of the Advanced Photon Source in Argonne National Laboratory. X-ray fluorescence from the NAC catalysts was collected using Lytle detector or 13-element Ge solid state detector. For each element, the corresponding reference metal foil was measured simultaneously in transmission mode. The Athena and Artemis programs of the Demeter package were used for EXAFS data processing and analysis. [29] $\chi(k)$ spectra representing the EXAFS oscillation were extracted by the embedded background removal method and then analyzed using the EXAFS equation. The first coordination shell after Fourier Transform was fitted using up to two single scattering paths (2 M-N paths or 1 M-N and 1 M-O) based on chemical information derived from XPS. The overall coordination number of the metal absorber was fixed at 4, and a common reduction factor S_0^2 and absorption edge correction dE_0 were used for two-shell fitting.

Electrode Preparation. 40 mg of the dried catalyst powder was ground with 4 mg polyvinylidene fluoride (PVDF) (industrial adhesive) with a few drops of 1-methyl-2-

pyrrolidone (MP) (solvent) to produce catalyst paste that was painted directly onto a 1.0 cm x 2.0 cm carbon paper (Toray TGP-H-060). The catalyst-decorated carbon paper was dried in a vacuum oven overnight and served as a working electrode. The deionized water was obtained from a Millipore Autopure System.

Electrochemical CO₂RR Test. Autolab electrochemical workstation was used to conduct CO₂ reduction experiments in aqueous 0.5 M KHCO₃. A platinum wire was used as counter electrode. All potentials were measured against an Ag/AgCl reference electrode (4.0 M KCl, Pine instrument) and were converted to those against a reversible hydrogen electrode (RHE). The experiments were performed in a gas-tight cell with two compartments separated by an anion exchange membrane (Nafion® 212). Each compartment contained 12 mL electrolyte with approximately 10 mL headspace.

Product Analysis. Before the experiment, the electrolyte in the cathode compartment was saturated with CO₂ by bubbling CO₂ gas for at least 30 min and was stirred at 900 rpm. CO₂ gas was delivered at an average rate of 10 mL/min (at room temperature and ambient pressure) and routed directly into the gas sampling loop of a gas chromatograph (SHIMADZU GC-2014). The gas phase composition was analyzed by GC every 35 min. The GC analysis was set up to split the gas sample into two aliquots whereof one aliquot was equipped with a thermal conductivity detector (TCD) for H₂ quantification. The second aliquot was equipped with a methanizer and a flame ionization detector (FID) for analyzing CO and C1 to C3 hydrocarbons. Argon (Corp Brother, 99.9999%) and hydrogen gas (Corp Brother, 99.9999%) were employed as carrier or make-up gases, respectively. ¹H NMR method was employed at the end of experiments to characterize liquid products. To be specific, 700 μL aliquot of the electrolyte was mixed with 70 μL dimethyl sulfoxide (DMSO) standard solution (20 mM DMSO in D₂O).
¹H NMR spectra were recorded on Varian NMRS 600 MHz.

DFT calculations. The DFT calculations were performed using the VASP package.^[30] The Perdew-Burke-Ernzerhof (PBE) functional within the generalized gradient approximation

(GGA) was used for the exchange-correlation energy. [31] Electron-ion interactions were described by the projector augmented wave (PAW) approach. [32] The van der Waals interaction was included using the DFT-D3 method. [33] All electronic energies were converged within 10^{-5} eV, and the force on each atom was optimized to be less than 0.02 eV Å-1. We calculated a 5×5 graphene surface with 20 Å vacuum in the z-direction. The $3\times 3\times 1$ Monkhorst-pack k-point mesh was used to sample the first Brillouin zone. We computed the Gibbs free energy of each elementary step using the computational hydrogen electrode model where the chemical potential of $(H^+ + e^-)$ at pH = 0 equals the chemical potential of 1 bar H_2 in the gas phase at 298 K. The zero-point energy and entropy change were calculated at 298 K derived from vibrational frequencies and statistical thermodynamics. We included entropic contribution during CO_2 adsorption and CO desorption by assuming the surface adsorbed species retain 2/3 of its gas-phase entropy. [34]

Supporting Information

Supporting Information is available from the Wiley Online Library or from the author.

Acknowledgements

Z.L. and L.Q. are supported by the U.S. Department of Energy (DOE), Office of Basic Energy Sciences, Division of Chemical Sciences, Geosciences, and Biosciences for the synthesis and characterization of the materials. All electron microscopy work was performed in the Sensitive Instrument Facility at Ames Laboratory, which is operated for the U.S. DOE by Iowa State University under Contract No. DE-AC02-07CH11358. Y. Z. and S. Z. acknowledge the support from US National Science Foundation (CBET-2004808) and 4-VA Collaborative Research Grant Program. W.H. thanks the support from the Trapp Award from Iowa State University. F.L. acknowledged the support from the Startup Fund at the University of Central Florida (UCF). B.H. is indebted to the funding support from the IRCCS of Hokkaido University. The

DFT calculations were supported by DOE, Office of Science, Office of Basic Energy Sciences, Catalysis Science Program, under Award No. DE-SC0018284, and performed using computational resources at the OU Supercomputing Center for Education & Research (OSCER) and the National Energy Research Scientific Computing Center (NERSC), a U.S. Department of Energy Office of Science User Facility. This research used resources of the Advanced Photon Source, a U.S. Department of Energy (DOE) Office of Science User Facility operated for the DOE Office of Science by Argonne National Laboratory under Contract No. DE-AC02-06CH11357. A.F.K. thanks the support from Science Undergraduate Laboratory Internship (SULI) program through Ames Laboratory, sponsored by U.S. Department of Energy Office of Science, and Office of Workforce Development for Teachers and Scientists (WDTS).

[+] These authors contributed equally to this work

References

- [1] a) Hironori Arakawa, Michele Aresta, John N. Armor, Mark A. Barteau, Eric J. Beckman, Alexis T. Bell, John E. Bercaw, Carol Creutz, Eckhard Dinjus, David A. Dixon, Kazunari Domen, Daniel L. DuBois, Juergen Eckert, Etsuko Fujita, Dorothy H. Gibson, William A. Goddard, D. Wayne Goodman, Jay Keller, Gregory J. Kubas, Harold H. Kung, James E. Lyons, Leo E. Manzer, Tobin J. Marks, Keiji Morokuma, Kenneth M. Nicholas, Roy Periana, Lawrence Que, Jens Rostrup-Nielson, Wolfgang M. H. Sachtler, Lanny D. Schmidt, Ayusman Sen, Gabor A. Somorjai, Peter C. Stair, and B. Ray Stults, W. Tumas, *Chem. Rev.* 2001, 101, 953. b) Toshiyasu Sakakura, and Jun-Chul Choi, H. Yasuda, *Chem. Rev.* 2007, 107, 2365. c) M. Mikkelsen, M. Jorgensen, F. C. Krebs, *Energy Environ. Sci.* 2010, 3, 43.
- [2] a) C. Tang, Y. Zheng, M. Jaroniec, S.-Z. Qiao, Angew. Chemie Int. Ed. 2021, 60, 19572. b) Genxiang Wang, Junxiang Chen, Yichun Ding, Pingwei Cai, Luocai Yi, Yan Li, Chaoyang Tu, Yang Hou, Zhenhai Wen, Liming Dai, Chem. Soc. Rev. 2021, 50, 4993.
- [3] a) M. Li, H. Wang, W. Luo, P. C. Sherrell, J. Chen, J. Yang, Adv. Mater. 2020, 32, 2001848. b) Y. Wang, H. Su, Y. He, L. Li, S. Zhu, H. Shen, P. Xie, X. Fu, G. Zhou, C. Feng, D. Zhao, F. Xiao, X. Zhu, Y. Zeng, M. Shao, S. Chen, G. Wu, J. Zeng, C. Wang, Chem. Rev. 2020, 120, 12217.
- [4] P. Su, K. Iwase, S. Nakanishi, K. Hashimoto, K. Kamiya, *Small* **2016**, *12*, 6083.
- [5] Y. Cheng, S. Zhao, H. Li, S. He, J. P. Veder, B. Johannessen, J. Xiao, S. Lu, J. Pan, M. F. Chisholm, S. Z. Yang, C. Liu, J. G. Chen, S. P. Jiang, *Appl. Catal. B Environ.* 2019, 243, 294.
- [6] T. Zheng, K. Jiang, N. Ta, Y. Hu, J. Zeng, J. Liu, H. Wang, *Joule* **2019**, *3*, 265.
- [7] H. Yang, Q. Lin, C. Zhang, X. Yu, Z. Cheng, G. Li, Q. Hu, X. Ren, Q. Zhang, J. Liu,C. He, *Nat. Commun.* 2020 111 2020, 11, 1.

- [8] H. M. T. Galvis, K. P. de Jong, ACS Catal. 2013, 3, 2130.
- [9] a) H. Zhang, Y. Zhang, Y. Li, S. Ahn, G. T. R. Palmore, J. Fu, A. A. Peterson, S. Sun, Nanoscale 2019, 11, 12075. b) K. J. P. Schouten, Z. Qin, E. P. Gallent, M. T. M. Koper, J. Am. Chem. Soc. 2012, 134, 9864.
- [10] J. Gu, C. S. Hsu, L. Bai, H. M. Chen, X. Hu, *Science* 2019, 364, 1091. b) C. Liu, Y.
 Wu, K. Sun, J. Fang, A. Huang, Y. Pan, W.C. Cheong, Z. Zhang, Z. Zhuang, Q. Yuan
 H.L. Xin, *Chem* 2021, 7, 1297. c) Z. Chen, A. Huang, K. Yu, T. Cui, Z. Zhuang, S.
 Liu, J. Li, R. Tu, K. Sun, X. Tan, J. Zhang, *Energy Environ. Sci.* 2021
- [11] Z. Chen, K. Mou, S. Yao, L. Liu, ChemSusChem 2018, 11, 2944.
- [12] Y. Pan, R. Lin, Y. Chen, S. Liu, W. Zhu, X. Cao, W. Chen, K. Wu, W.-C. Cheong, Y.
 Wang, L. Zheng, J. Luo, Y. Lin, Y. Liu, C. Liu, J. Li, Q. Lu, X. Chen, D. Wang, Q.
 Peng, C. Chen, Y. Li, *J. Am. Chem. Soc.* 2018, *140*, 4218.
- [13] H. Yang, Y. Wu, G. Li, Q. Lin, Q. Hu, Q. Zhang, J. Liu, C. He, J. Am. Chem. Soc.2019, 141, 12717.
- [14] a) W. Ju, A. Bagger, G. P. Hao, A. S. Varela, I. Sinev, V. Bon, B. Roldan Cuenya, S. Kaskel, J. Rossmeisl, P. Strasser, *Nat Commun* 2017, 8, 944. b)X.-M. Hu, H. H. Hval, E. T. Bjerglund, K. J. Dalgaard, M. R. Madsen, M.-M. Pohl, E. Welter, P. Lamagni, K. B. Buhl, M. Bremholm, M. Beller, S. U. Pedersen, T. Skrydstrup, K. Daasbjerg, *ACS Catal.* 2018, 8, 6255. c) Z. Li, Y. Chen, S. Ji, Y. Tang, W. Chen, A. Li, J. Zhao, Y. Xiong, Y. Wu, Y. Gong, T. Tao, *Nat. Chem.* 2020 12 764. d) W. Zheng, F. Chen, Q. Zeng, Z. Li, B. Yang, L. Lei, Q. Zhang, F. He, X. Wu, Y. Hou, *Nanomicro Lett.* 2020 12 1.
- [15] F. Pan, W. Deng, C. Justiniano, Y. Li, *Appl. Catal. B Environ.* **2018**, *226*, 463.
- [16] W. Bi, X. Li, R. You, M. Chen, R. Yuan, W. Huang, X. Wu, W. Chu, C. Wu, Y. Xie, Adv. Mater. 2018, 30, 1706617.

- [17] P. Paoletti, Pure Appl. Chem. **1984**, 56, 491.
- [18] Z. Luo, R. Nie, V. T, Nguyen, A. Biswas, R. K. Behera, X. Wu, T. Kobayashi, A. Sadow, B. Wang, W. Huang, L. Qi, *Nat. Commun.* **2020**, *11*, 1-9.
- [19] Jincheng Zhang, Weizheng Cai, F. Xin Hu, Hongbin Yang, Bin Liu, *Chem. Sci.* **2021**, *12*, 6800.
- [20] a)M. Ayiania, M. Smith, A. J. R. Hensley, L. Scudiero, J. S. McEwen, M. Garcia-Perez, *Carbon N. Y.* 2020, *162*, 528. b)G. Greczynski, L. Hultman, *Angew. Chemie* 2020, *132*, 5034.
- [21] G. Li, H. Yang, H. Zhang, Z. Qi, M. Chen, W. Hu, L. Tian, R. Nie, W. Huang, *ACS Catal.* **2018**, *8*, 8396.
- [22] Z. Luo, R. Nie, V. T. Nguyen, A. Biswas, R. K. Behera, X. Wu, T. Kobayashi, A. Sadow, B. Wang, W. Huang, L. Qi, *Nat. Commun.* **2020**, *11*, 1.
- [23] a)McKeown, N. B., Phthalocyanine materials: synthesis, structure, and function.
 Cambridge University Press: Cambridge, U.K.; New York, 1998. b) K. M. Barkigia,
 M. W. Renner, L. R. Furenlid, C. J. Medforth, K. M. Smith, J. Fajer, J. Am. Chem. Soc.
 2002, 115, 3627.
- [24] a) Zoltán Németh, É. G. Bajnóczi, Bogdán Csilla, György Vankó, *Phys. Chem. Chem. Phys.* 2019, 21, 9239. b) V. V. Pavlishchuk, S. V. Kolotilov, A. W. Addison, R. J. Butcher, Ekkehard Sinn, *J. Chem. Soc. Dalt. Trans.* 2000, 0, 335.
- [25] M. Karppinen, H. Yamauchi, Y. Yasukawa, J. Lindén, T. S. Chan, and R. S. Liu, J. M. Chenl, *Chem. Mater.* 2003, 15, 4118.
- [26] N. Kosugi, T. Yokoyama, K. Asakura, H. Kuroda, *Chem. Phys.* **1984**, *91*, 249.
- [27] Z. Yin, G. T. R. Palmore, S. Sun, *Trends Chem.* **2019**, *1*(8), 739
- [28] a) C. Zhao, Y. Wang, Z. Li, W. Chen, Q. Xu, D. He, D. Xi, Q. Zhang, T. Yuan, Y. Qu, J. Yang, F. Zhou, Z. Yang, X. Wang, J. Wang, J. Luo, Y. Li, H. Duan, Y. Wu, Y. Li, *Joule* 2019, 3, 584. b) Q. He, D. Liu, J. H. Lee, Y. Liu, Z. Xie, S. Hwang, S. Kattel, L.

- Song, J. G. Chen, *Angew. Chemie Int. Ed.* **2020**, *59*, 3033. c) C. Xu, X. Zhi, A. Vasileff, D. Wang, B. Jin, Y. Jiao, Y. Zheng, S.-Z. Qiao, *Small Struct.* **2021**, *2*, 2000058.
- [29] B. Ravel, M. Newville, IUCr, urn:issn:0909-0495 2005, 12, 537.
- [30] G. Kresse, J. Furthmüller, *Phys. Rev. B* **1996**, *54*, 11169.
- [31] J. P. Perdew, K. Burke, M. Ernzerhof, Phys. Rev. Lett. 1996, 77, 3865.
- [32] P. E. Blöchl, *Phys. Rev. B* **1994**, *50*, 17953.
- [33] S. Grimme, J. Antony, S. Ehrlich, H. Krieg, J. Chem. Phys. 2010, 132, 154104.
- [34] C. T. Campbell, J. R. V. Sellers, J. Am. Chem. Soc. 2012, 134, 18109.

Zhicheng Luo+, Zhouyang Yin+, Jiaqi Yu, Yu Yan, Bing Hu, Renfeng Nie, Anna F. Kolln, Xun Wu, Ranjan K Behera, Minda Chen, Lin Zhou, Fudong Liu, Bin Wang, Wenyu Huang,* Sen Zhang,* Long Qi*

General Strategy to Synthesize High Surface-Area Catalysts with Single-atom Metals for Electrochemical CO₂ Reduction



Benchmark study of various single-atom transition metal catalysis is achieved for electrochemical reduction of CO₂ to CO. The single-atom Ni anchored on ordered mesoporous nitrogen assembly carbon catalyst, Ni-NAC, possesses not only high CO selectivity and current density but also high durability in a broad potential range.

Supporting Information

General Synthetic Strategy to Ordered Mesoporous Carbon Catalysts with Single-Atom Metal Sites for Electrochemical CO₂ Reduction

Zhicheng Luo⁺, Zhouyang Yin⁺, Jiaqi Yu, Yu Yan, Bing Hu, Renfeng Nie, Anna F. Kolln, Xun Wu, Ranjan K Behera, Minda Chen, Lin Zhou, Fudong Liu, Bin Wang, Wenyu Huang,* Sen Zhang,* Long Qi*

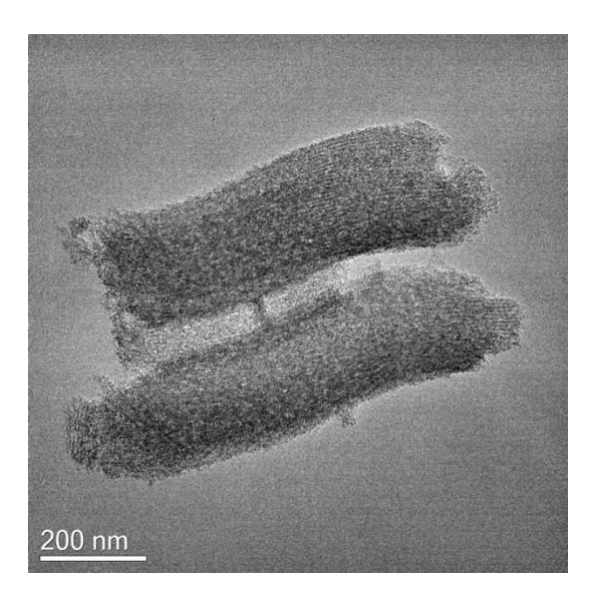


Figure S1. Low magnification TEM image of Ni-NAC.

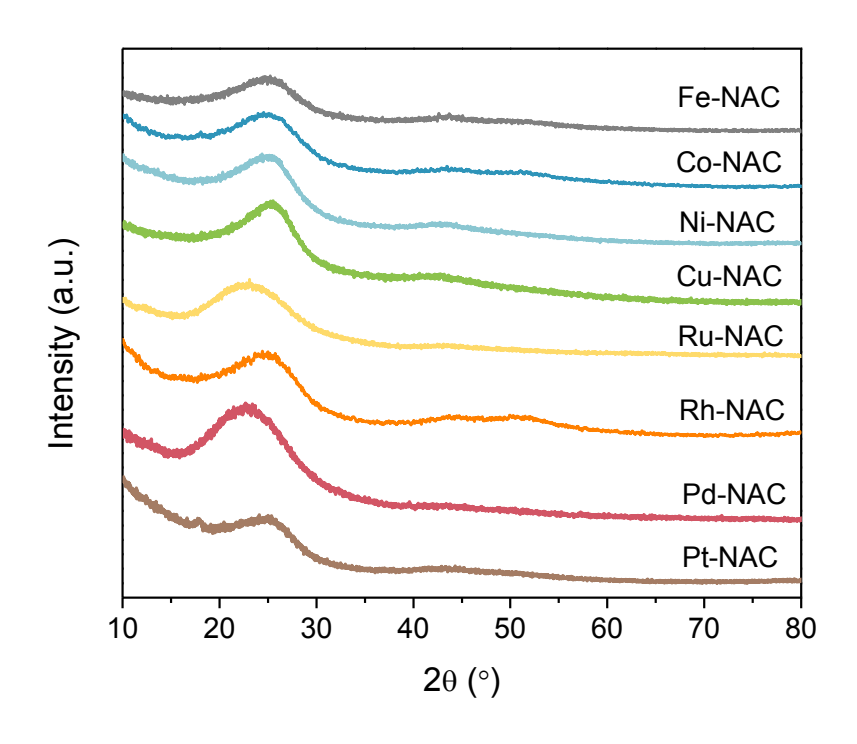


Figure S2. XRD patterns of M-NACs.

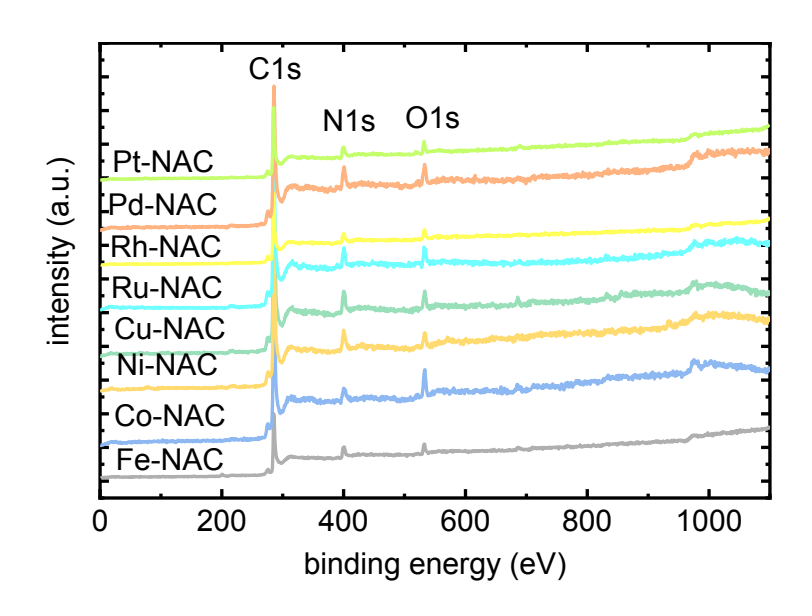


Figure S3. XPS wide-scan spectra of M-NACs.

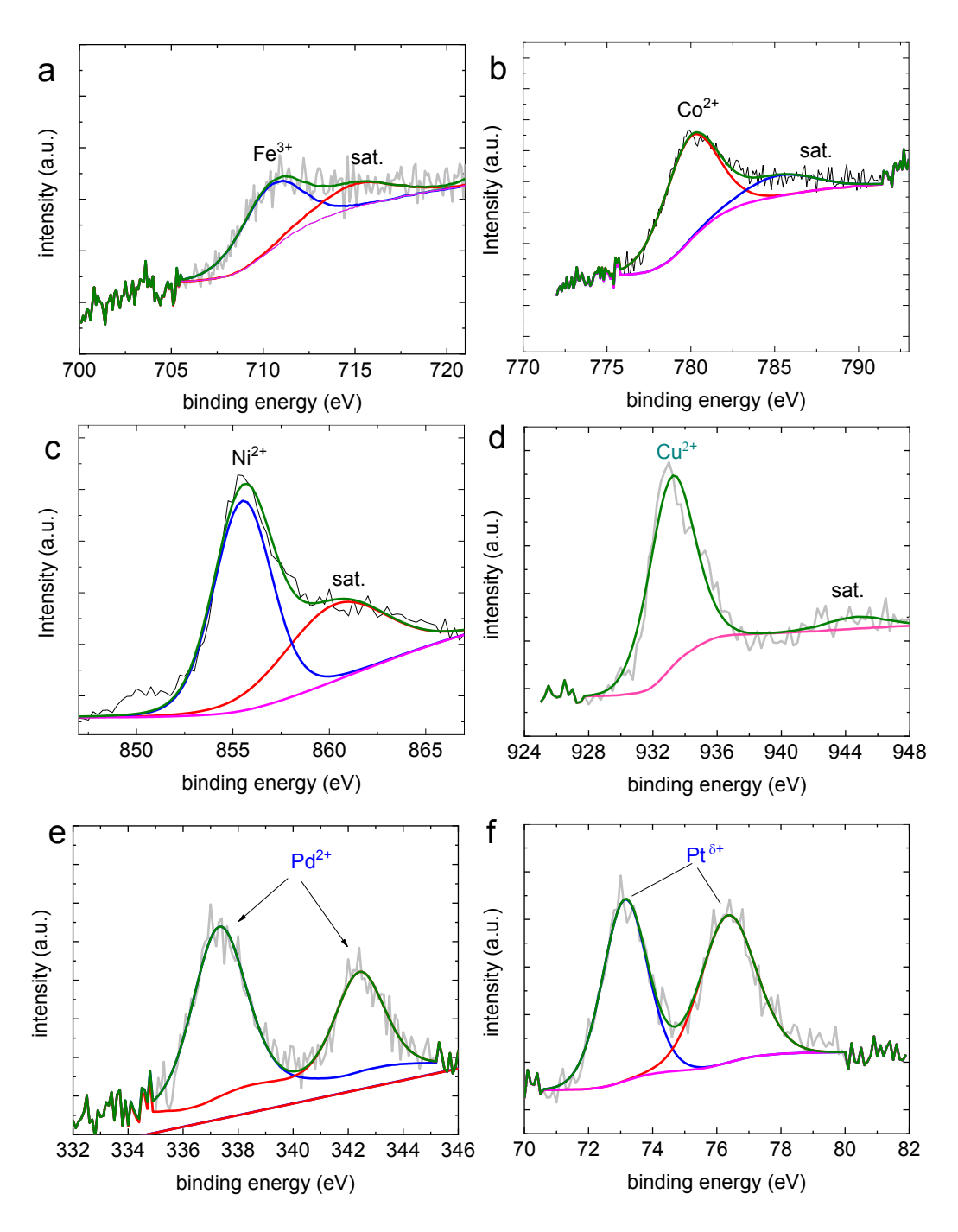


Figure S4. The XPS spectra for corresponding metal species in the M-NACs. The spectra for Ru and Rh are not shown due to the strong overlapping of Ru3d and Rh3d with C1s regions.

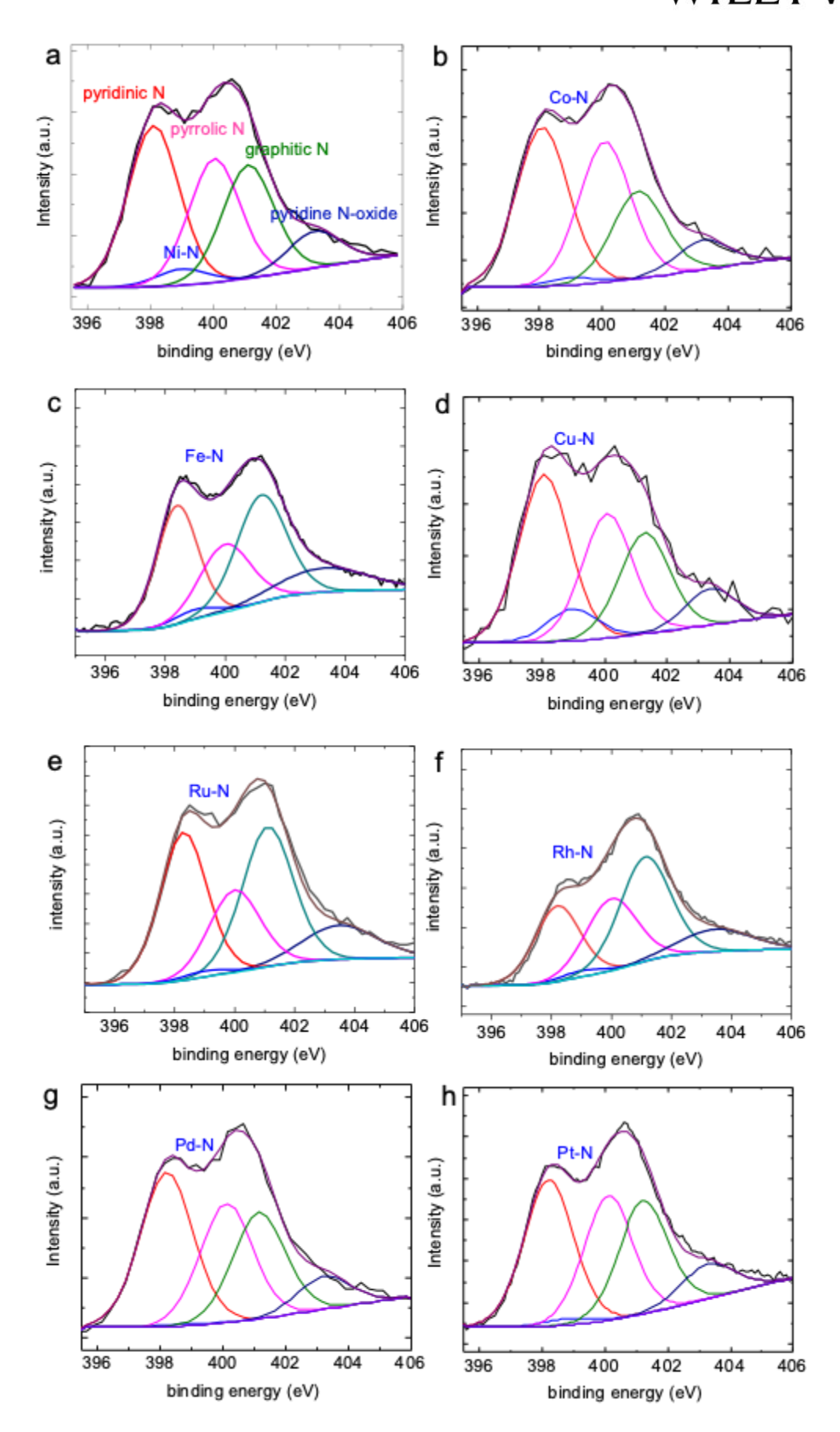


Figure S5. N1s XPS spectra of M-NACs. The pyridinic N, M-N, pyrrolic N, graphitic N, and pyridinic N-oxide are color-coded in red, blue, pink, green, and navy, respectively.

 Table S1. BET analysis of M-NACs.

entry	samples	$S_{ m BET}$	V _{pore} (cm ³ /g)	D_{p}
		(m^2/g)		(nm)
1	Fe-NAC	771	0.66	3.4
2	Co-NAC	823	0.61	3.7
3	Ni-NAC	822	0.65	3.4
4	Cu-NAC	872	0.75	3.5
5	Ru-NAC	760	1.18	3.6
6	Rh-NAC	995	0.95	3.8
7	Pd-NAC	809	0.97	3.8
8	Pt-NAC	928	1.08	3.8

Table S2. XPS, elemental analysis and ICP of M-NACs.

	_		XPS			CHN		ICP
	samples	C(at%)	N(at%)	C:N (atomic)	C(wt%)	N(wt%)	C:N (atomic)	metal (wt%)
1	Fe-NAC	81.0	11.7	6.9	66.60	12.15	6.4	0.7
2	Co-NAC	81.9	10.9	7.5	63.58	12.43	6.0	1.6
3	Ni-NAC	84.6	9.4	9.0	65.21	11.17	6.8	1.7
4	Cu-NAC	84.4	11.4	7.4	64.79	11.77	6.4	4.2
5	Ru-NAC	86.7	9.2	9.6	70.91	12.17	6.8	0.2
6	Rh-NAC	82.1	11.8	7.0	73.27	12.22	7.0	0.1*
7	Pd-NAC	79.7	8.8	9.1	70.28	12.46	6.6	0.5
8	Pt-NAC	83.1	11.0	7.6	73.30	12.32	6.9	1.0

^{*} Estimated based on XPS rather than ICP-MS.

Table S3. N1s fitting data of M-NACs.

ontra	catalysts	N species (%)					
entry		pyridinic N	M-N	pyrrolic N	graphitic N	pyridine N-oxide	
1	Fe-NAC	31.14	1.77	28.77	28.29	10.04	
2	Co-NAC	43.21	1.62	25.59	21.97	7.61	
3	Ni-NAC	35.59	3.60	27.34	25.03	8.44	
4	Cu-NAC	34.95	2.66	21.79	27.21	13.40	
5	Ru-NAC	33.17	1.32	19.85	33.84	11.83	
6	Rh-NAC	24.18	1.95	25.66	37.16	11.06	
7	Pd-NAC	40.07	0.91	29.44	24.94	4.63	
8	Pt-NAC	34.13	1.55	29.11	26.56	8.66	

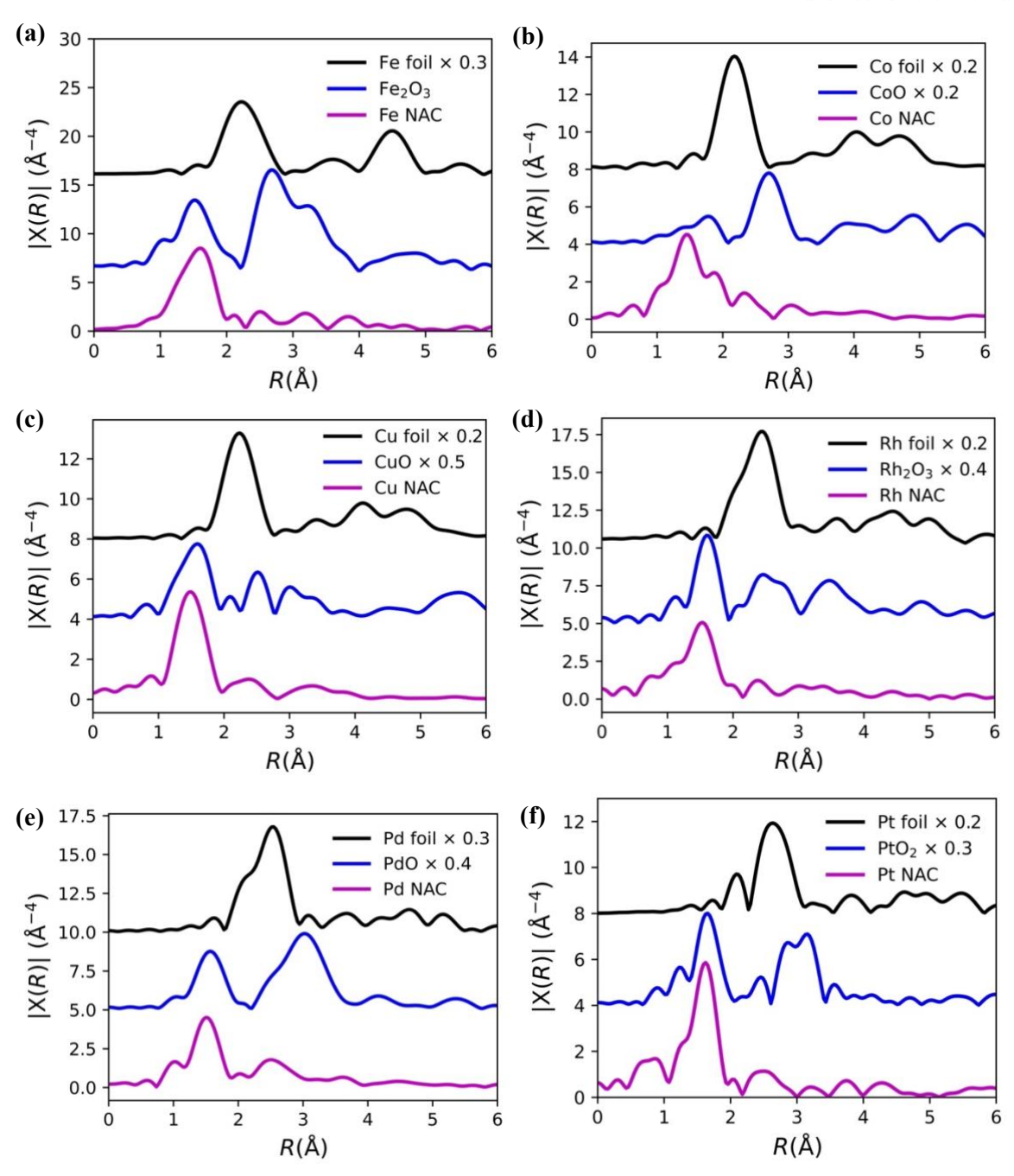


Figure S6. R-space plots of metal K-edge (L3-edge for Pt) EXAFS of (a) Fe-NAC, (b) Co-NAC, (c) Cu-NAC, (d) Rh-NAC, (e) Pd-NAC, and (f) Pt-NAC in comparison with those of the corresponding metal foil and metal oxide reference standards after Fourier transform of k^3 -weighted $\chi(k)$ of the same k range.

Figure S7. Best-fit parameters from the peak fitting analysis of the Fe-NAC K-edge EXAFS spectra. CN is the coordination number, d is the bond length, DW2 is the Debye-Waller factor, S_0^2 is the amplitude reduction factor, and R-factor is the percentage misfit between theory and data

k-range: 2.5-12.0 Å $^{-1}$ R-range: 1.0-2.3 Å $N_{param}/N_{indp} = 6/8$

	CN	d (Å)	dE _o (eV)	DW ² (Å ²)	S ₀ ²	R-factor (%)
Fe-O	1.0	1.86±0.02 2.03±0.01	0.3±1.1	0.0012±0.0036 0.0042±0.0024	1.22±0.13	0.5
Fe-N	4.0	2.03 ± 0.01	0.3±1.1	0.0042 ± 0.0024	1.22±0.13	0.3

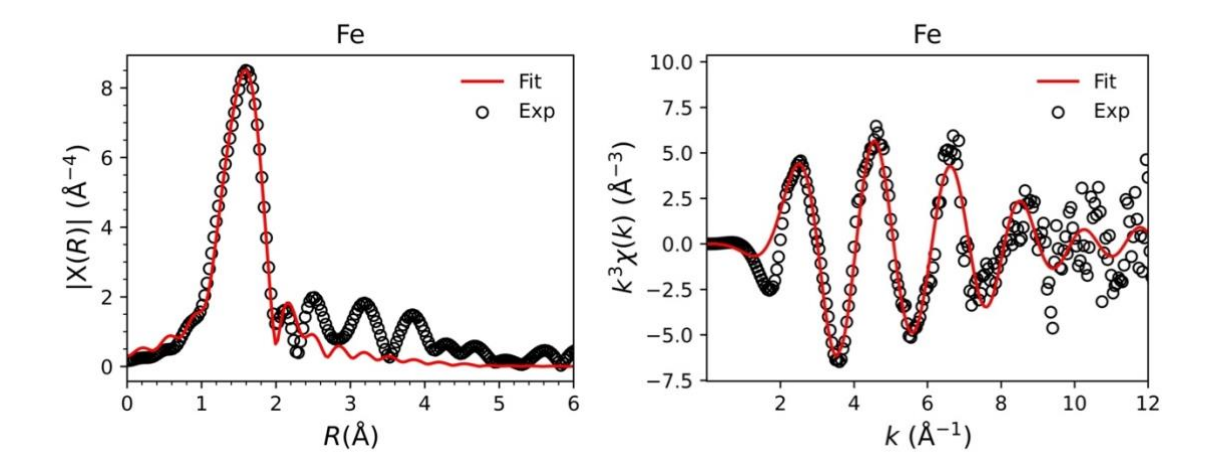


Figure S8. Best-fit parameters from the peak fitting analysis of the Co-NAC K-edge EXAFS spectra.

k-range: $2.5-12.0\text{Å}^{-1}$ R-range: 0.8-2.8Å $N_{param}/N_{indp} = 6/12$

	CN	d (Å)	dE _o (eV)	DW ² (Å ²)	S ₀ ²	R-factor (%)
CoN1 CoN2	2.0 2.0	1.91±0.01 2.10±0.01	10.3±0.8	0.0045±0.0017 0.0058±0.0023	1.14±0.09	1.1

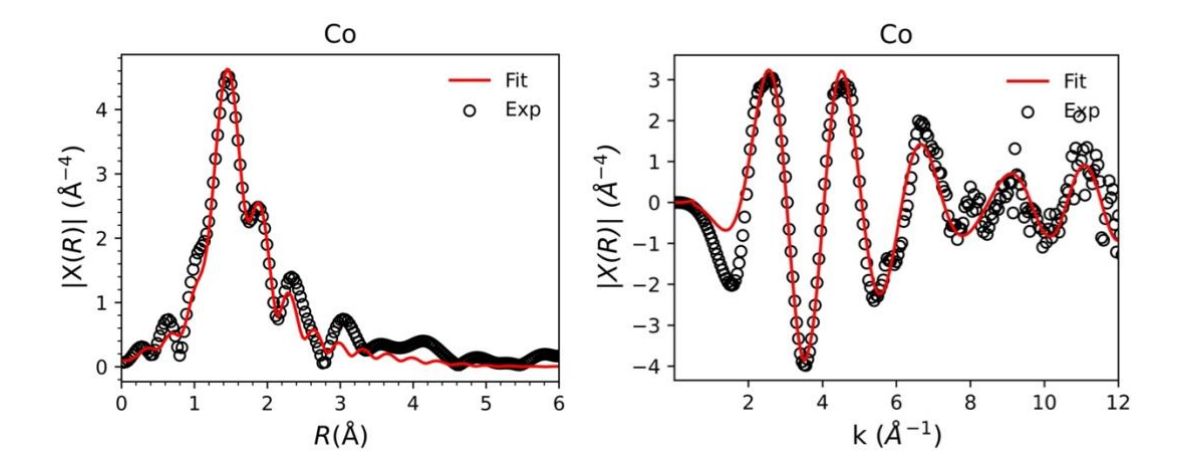


Figure S9. Best-fit parameters from the peak fitting analysis of the Ni-NAC K-edge EXAFS spectra using two single scattering paths of Ni-N with different bond length.

k-range: $3.0-12.0\text{Å}^{-1}$ R-range: 1.0-3.0Å N_{param}/N_{indp} = 6/12

	CN	d (Å)	dE _o (eV)	$\overline{\mathrm{DW}^{2}}(\mathring{\mathrm{A}}^{2})$	S ₀ ²	R-factor (%)
Ni-N1 Ni-N2	2.0 2.0	1.87±0.01 2.05±0.02	-3.2±1.2	0.0024±0.0015 0.0048±0.0022	1.19±0.13	1.3

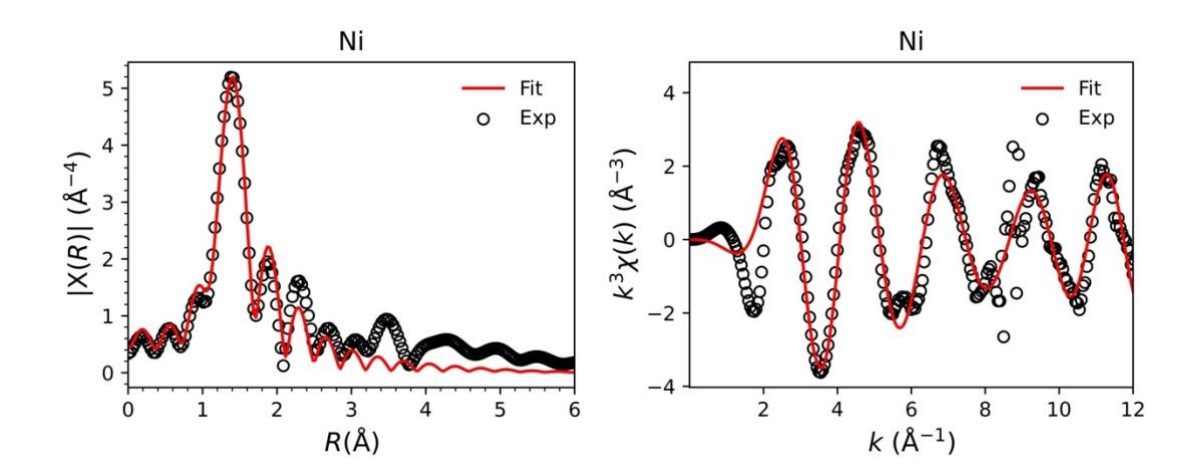


Figure S10. Best-fit parameters from the peak fitting analysis of the Ni-NAC K-edge EXAFS spectra using the three single scattering paths of Ni-N1, Ni-N2, and Ni-C.

k-range: $3.0-12.0\text{Å}^{-1}$ R-range: 1.0-2.5Å $N_{param}/N_{indp} = 8/9$

	CN	d (Å)	dE _o (eV)	DW ² (Å ²)	S_0^2	R-factor (%)
Ni-N1	1.0	2.02 ± 0.04		0.0020 ± 0.0026		
Ni-N2	2.0	1.86 ± 0.02	-3.4 ± 1.8	0.0019 ± 0.0022	1.06 ± 0.15	1.3
Ni-C	1.0	2.12 ± 0.04		0.0037 ± 0.0052		

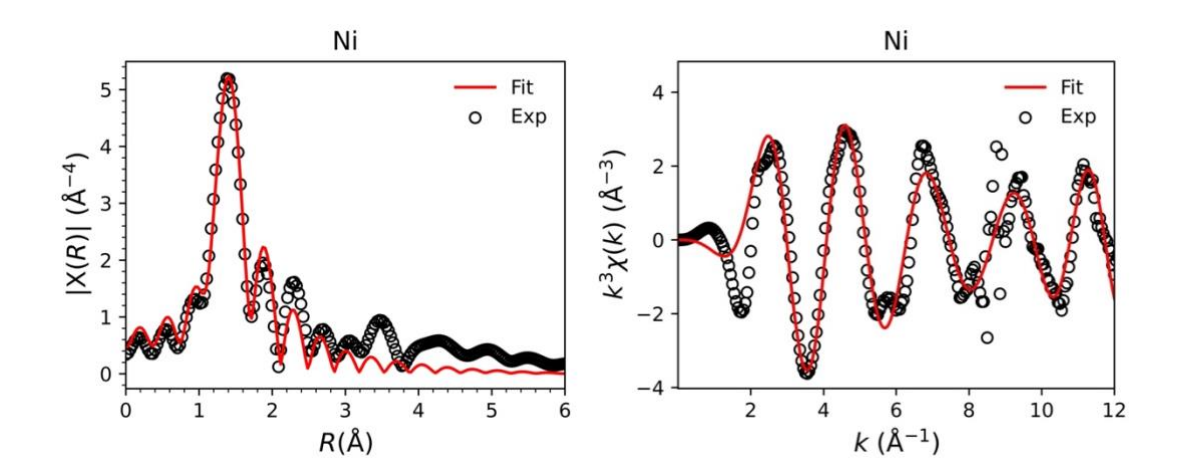


Figure S11. Best-fit parameters from the peak fitting analysis of the Cu-NAC K-edge EXAFS spectra using a single Cu-N path.

Cu		Cu
5 (A-A) (A-A) (A-A) 1 0 0 0 0 0 0 0 0 0 0 0 0 0 0 0 0 0 0	Fit 3- 0 Exp 2- $(Y)(Y)(Y)$ $(Y)(Y)$ $(Y)(Y)(Y)$ $(Y)(Y)(Y)(Y)$ $(Y)(Y)(Y)(Y)(Y)$ $(Y)(Y)(Y)(Y)(Y)(Y)$ $(Y)(Y)(Y)(Y)(Y)(Y)$ $(Y)(Y)(Y)(Y)(Y)(Y)$ $(Y)(Y)(Y)(Y)(Y)(Y)$ $(Y)(Y)(Y)(Y)(Y)(Y)(Y)$ $(Y)(Y)(Y)(Y)(Y)(Y)(Y)$ $(Y)(Y)(Y)(Y)(Y)(Y)(Y)(Y)$ $(Y)(Y)(Y)(Y)(Y)(Y)(Y)(Y)(Y)$ $(Y)(Y)(Y)(Y)(Y)(Y)(Y)(Y)(Y)(Y)$ $(Y)(Y)(Y)(Y)(Y)(Y)(Y)(Y)(Y)(Y)(Y)(Y)(Y)($	o Fit exp
0 1 2 3 R(Å)	4 5 6	$k (\mathring{A}^{-1})$

Figure S12. Best-fit parameters from the peak fitting analysis of the Cu-NAC K-edge EXAFS spectra using two single scattering paths of Cu-N and Cu-C.

k-range: 3.0-12.0 Å ⁻¹ R-range: 1.0-2.8 Å $N_{param}/N_{indp} = 5/11$

	CN	d (Å)	dE _o (eV)	DW ² (Å ²)	S_0^2	R-factor (%)
Cu-N	3.0	1.93±0.01	5.6±1.3	0.0052±0.0012	1.00*	1.2
Cu-C	1.0	2.09 ± 0.04	3.0±1.3	0.0025 ± 0.0034	1.00	1.4

^{*}Fixed

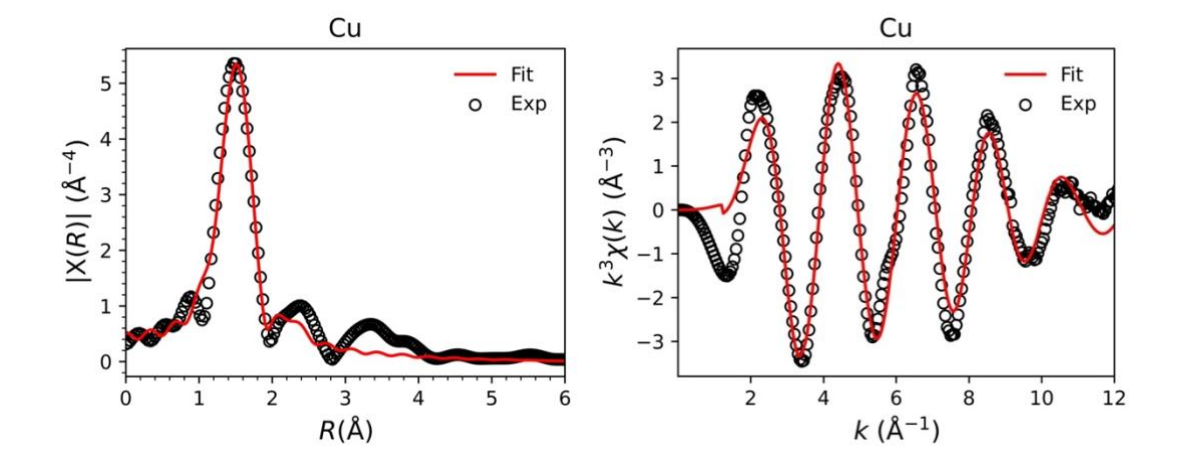


Figure S13. Best-fit parameters from the peak fitting analysis of the Ru-NAC K-edge EXAFS spectra.

k-range: 3.0-12.0 Å ⁻¹ R-range: 1.0-2.7 Å $N_{param}/N_{indp} = 6/10$

	CN	d (Å)	dE _o (eV)	DW ² (Å ²)	S_0^2	R-factor (%)
Ru-O Ru-N	1.0 4.0	1.86±0.04 2.03±0.02	-4.5±2.3	0.0021±0.0066 0.0029±0.0032	0.85±0.19	2.7

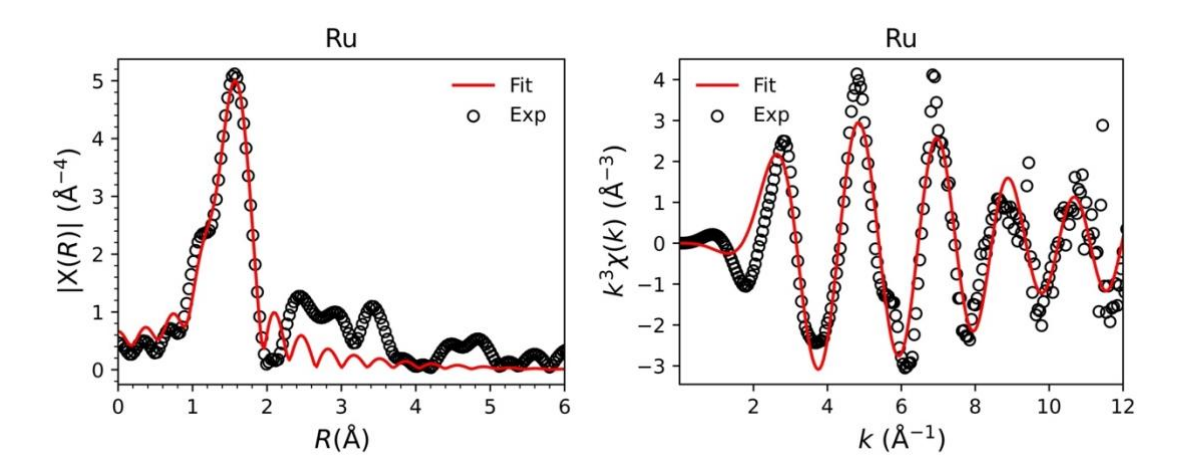


Figure S14. Best-fit parameters from the peak fitting analysis of the Rh-NAC K-edge EXAFS spectra.

k-range: $3.0-12.0\text{Å}^{-1}$ R-range: 1.0-2.1Å N_{param}/N_{indp} = 4/7

	CN	d (Å)	dE _o (eV)	DW ² (Å ²)	S_0^2	R-factor (%)
RhN	4.0	2.02±0.02	-3.2±2.2	0.0081±0.0023	1.10±0.17	2.2

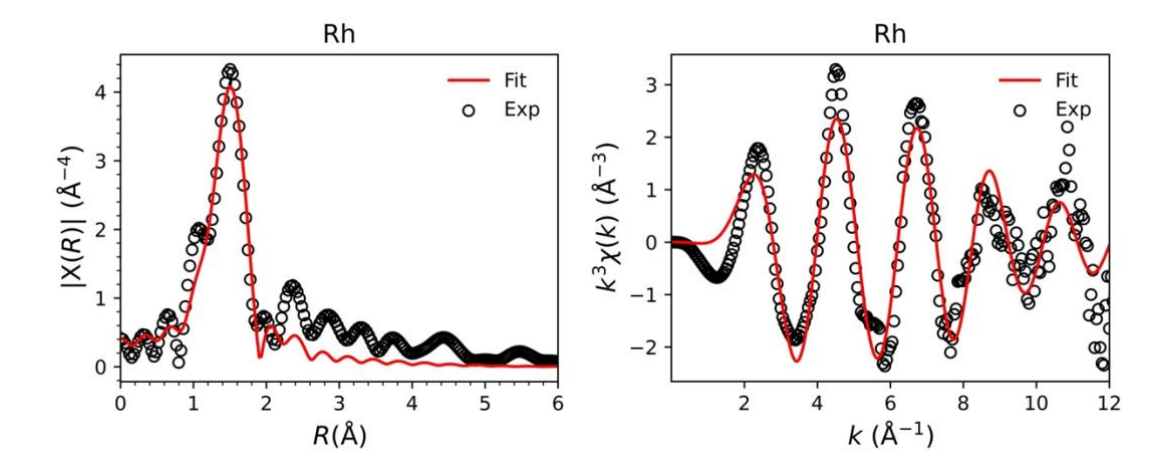


Figure S15. Best-fit parameters from the peak fitting analysis of the Pd-NAC K-edge EXAFS spectra.

k-range: $3.0-12.0\text{Å}^{-1}$ R-range: 1.0-2.2Å $N_{param}/N_{indp} = 4/7$

	CN	d (Å)	dE _o (eV)	DW ² (Å ²)	S_0^2	R-factor (%)
PdN	4.0	1.98±0.01	-0.6±1.2	0.0035±0.0010	0.68 ± 0.06	0.7

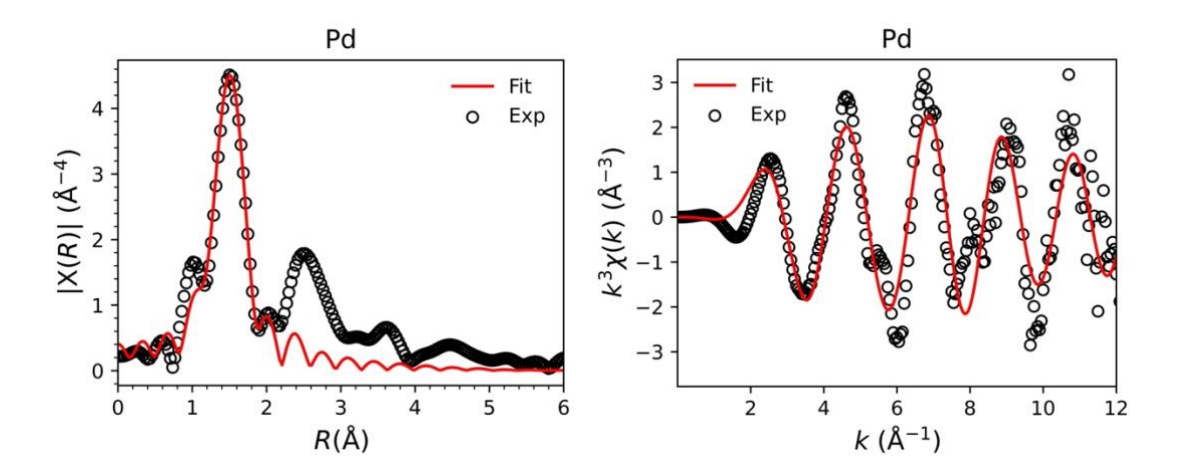


Figure S16. Best-fit parameters from the peak fitting analysis of the Pt-NAC L3-edge EXAFS spectra using a Pt-N single scattering paths.

k-range: $3.0-12.0\text{Å}^{-1}$ R-range: 1.1-2.2Å $N_{param}/N_{indp} = 4/7$

	CN	d (Å)	dE _o (eV)	DW ² (Å ²)	S ₀ ²	R-factor (%)
PtN	4.0	1.98 ± 0.01	7.9±1.7	0.0058 ± 0.0020	0.90 ± 0.13	1.2

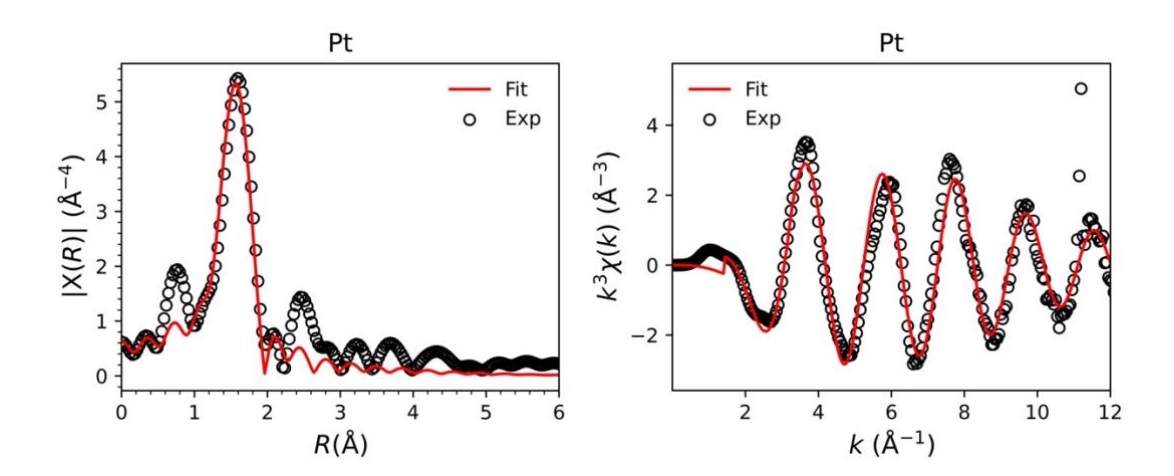
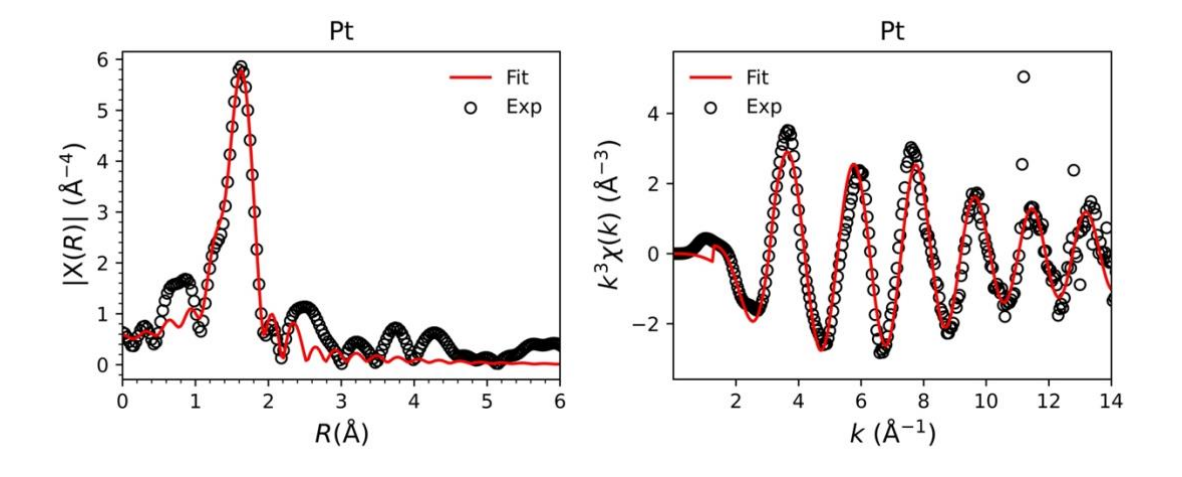


Figure S17. Best-fit parameters from the peak fitting analysis of the Pt-NAC L3-edge EXAFS spectra using two single scattering paths of Pt-N and Pt-C.

k-range: $3.0-14.0\text{\AA}^{-1}$ R-range: 1.1-2.2Å $N_{param}/N_{indp} = 5/8$

	CN	d (Å)	dE _o (eV)	DW ² (Å ²)	S ₀ ²	R-factor (%)
PtC	1.0	1.88 ± 0.03	6.1±1.3	0.0016±0.0033	1.00*	0.4
PtN	3.0	1.99 ± 0.01	0.1±1.3	0.0023 ± 0.0013	1.00	0.4

^{*}Fixed



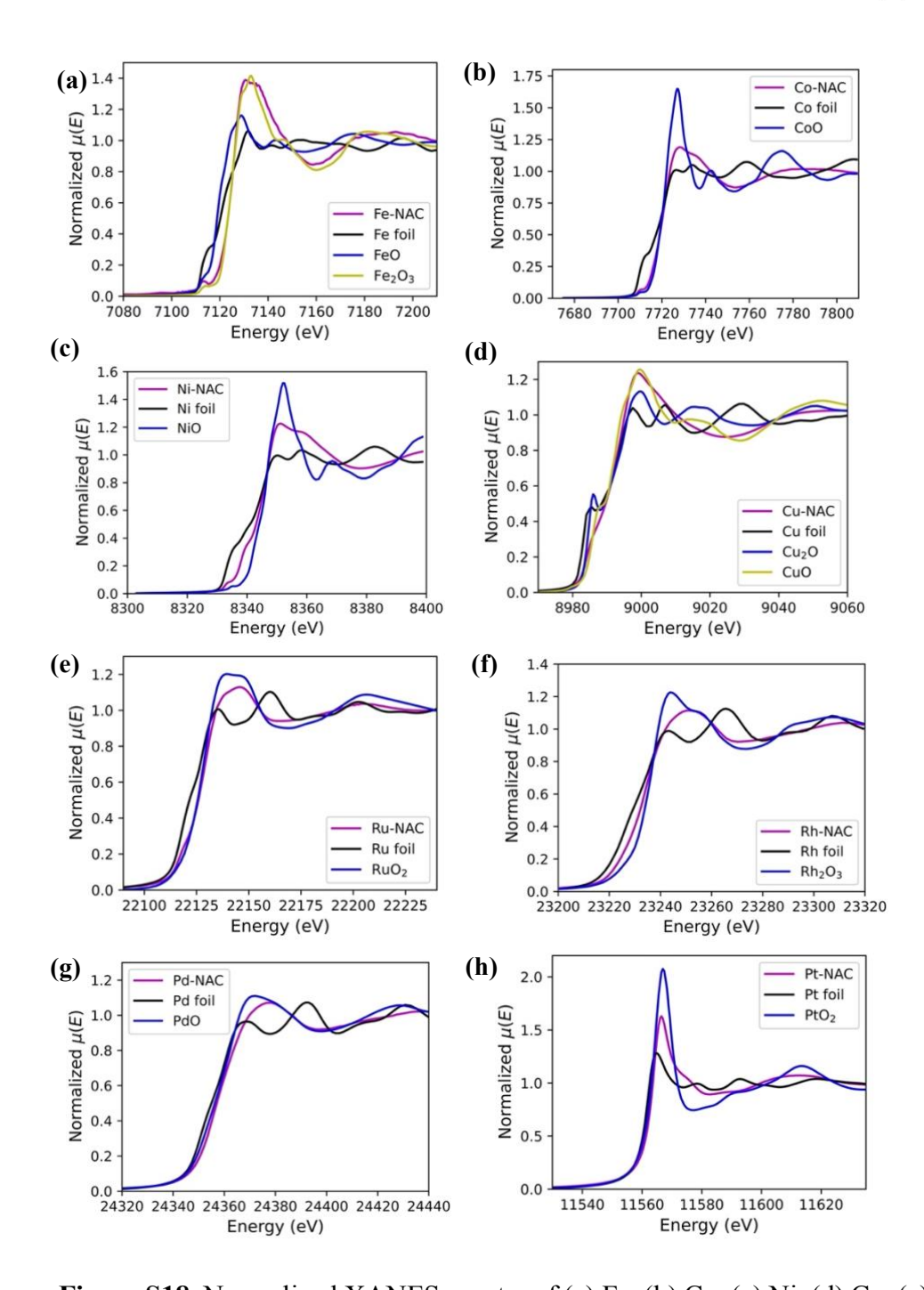


Figure S18. Normalized XANES spectra of (a) Fe, (b) Co, (c) Ni, (d) Cu, (e) Ru, (f) Rh, (g) Pd K edges and (h) Pt L3 edge of the M-NACs and corresponding metal foil and metal oxides.

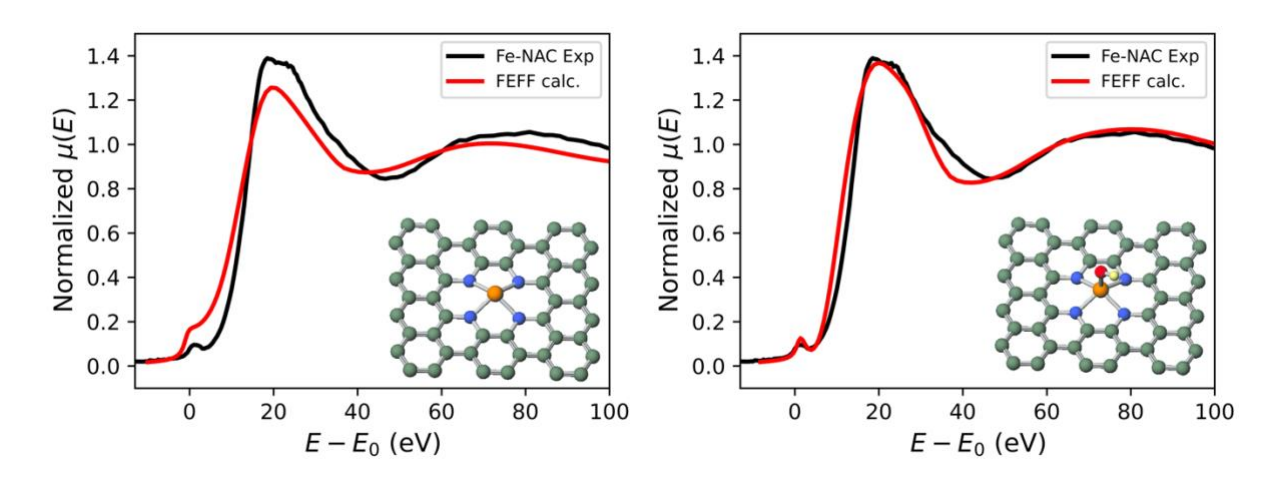


Figure S19. XANES simulation of Fe-NAC using a non-planar PtN₄ (left) moiety in comparison with PtN₄(OH) (right). The grayish green atom is C, blue is N, red is O, yellow is H, and the colored single atom in the center is the metal atom (the same for the other figures of XANES simulation).

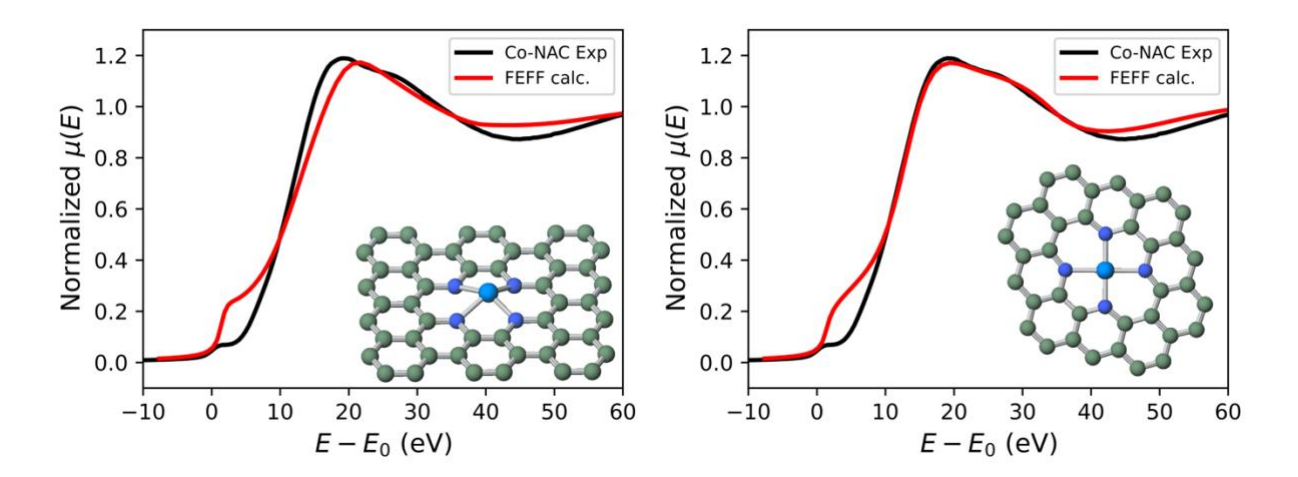


Figure S20. XANES simulation of Co-NAC.

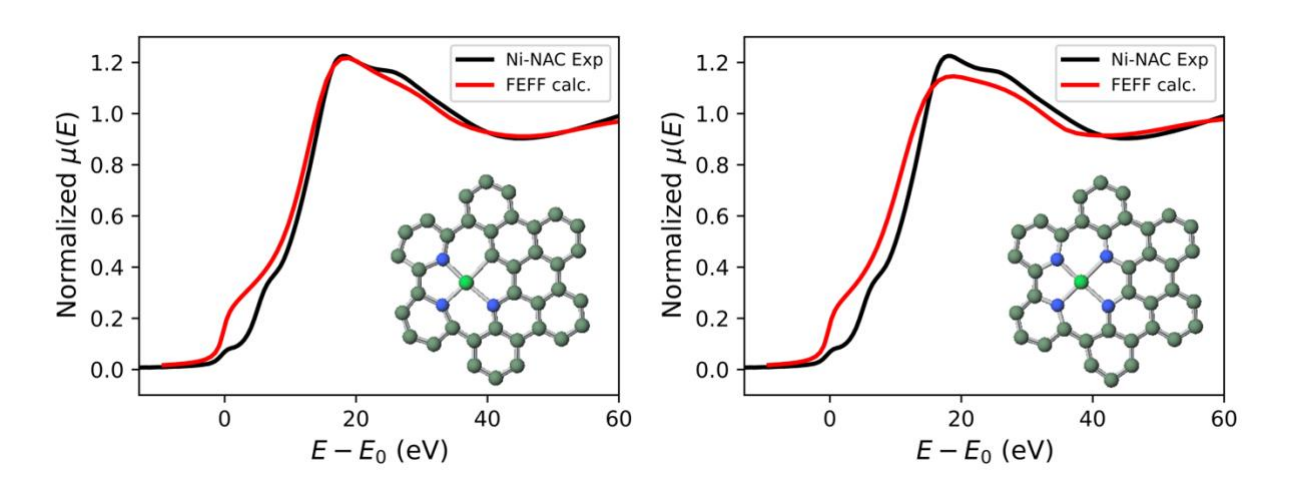


Figure S21. XANES simulation of Ni-NAC.

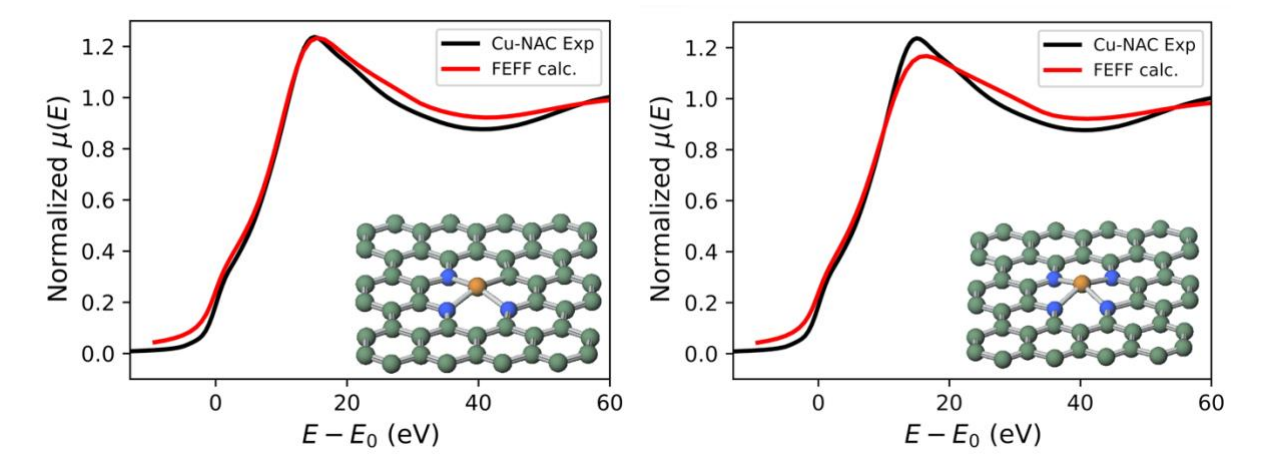


Figure S22. XANES simulation of Cu-NAC.

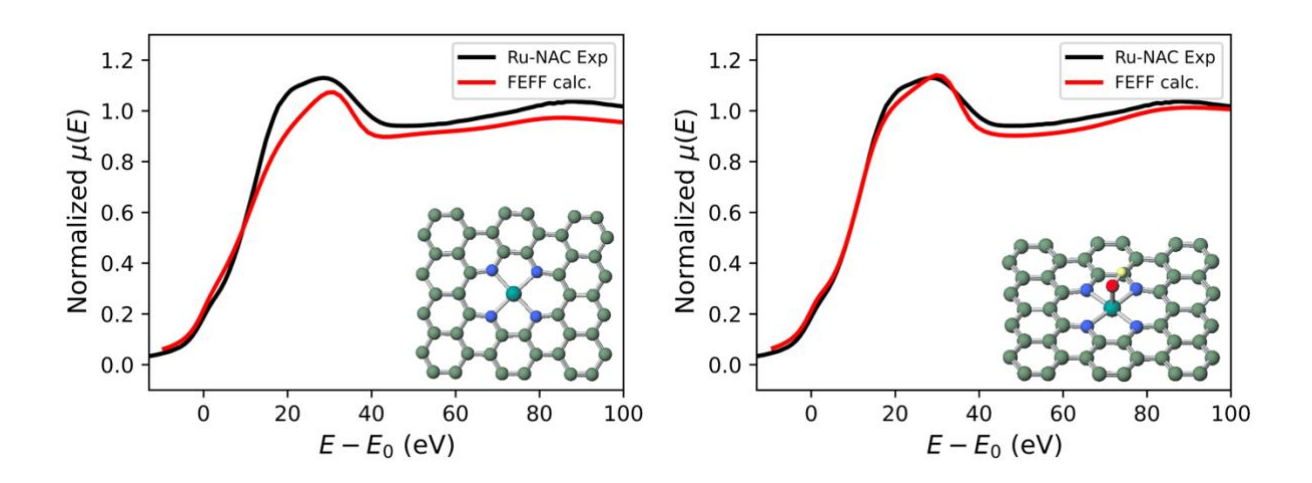


Figure S23. XANES simulation of Ru-NAC.

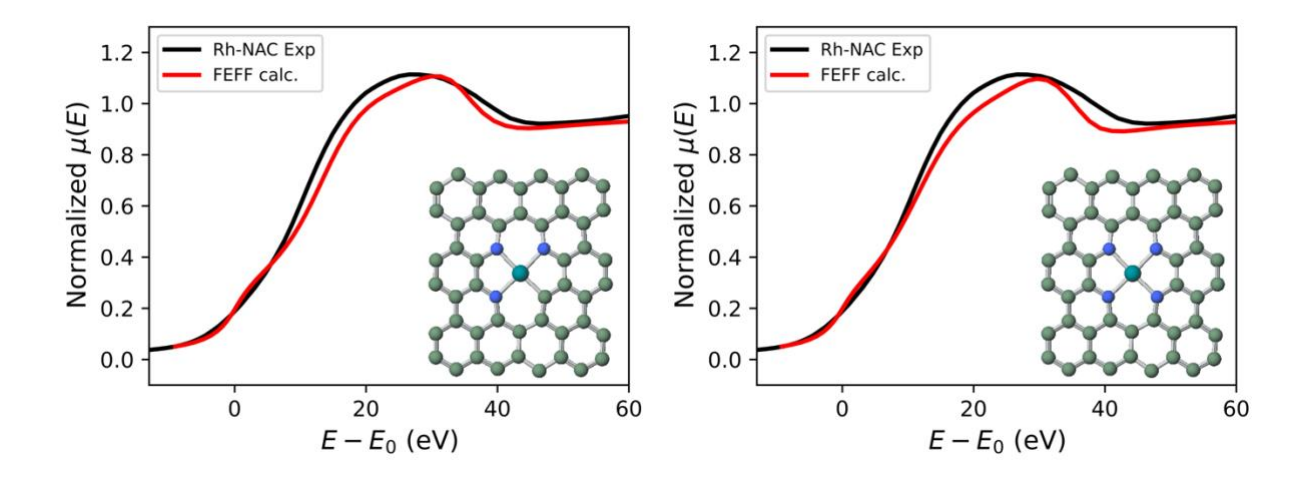


Figure S24. XANES simulation of Rh-NAC.

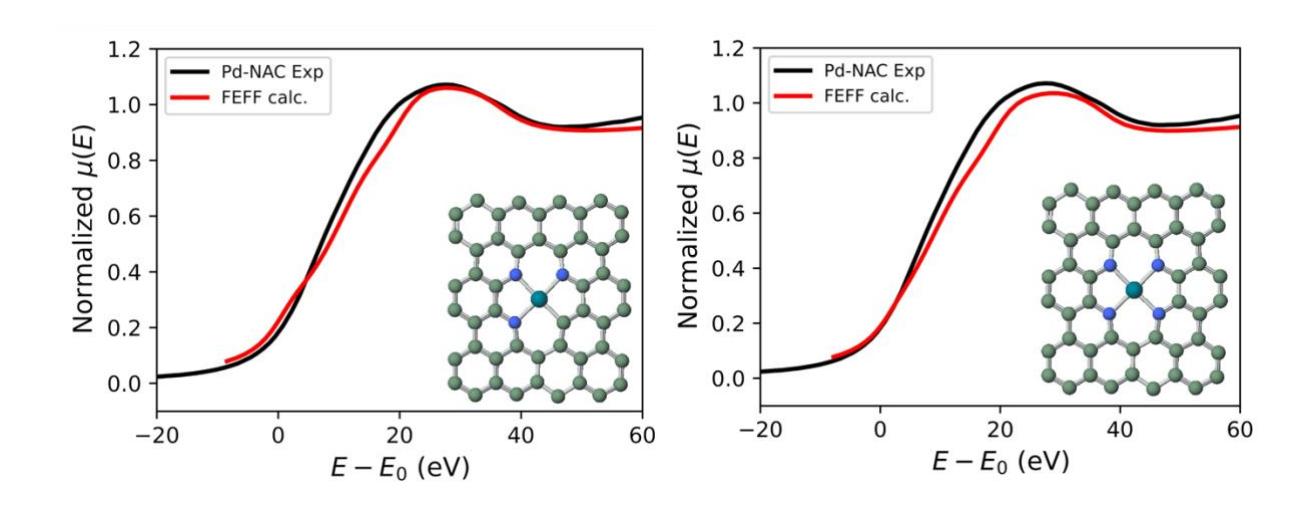


Figure S25. XANES simulation of Pd-NAC.

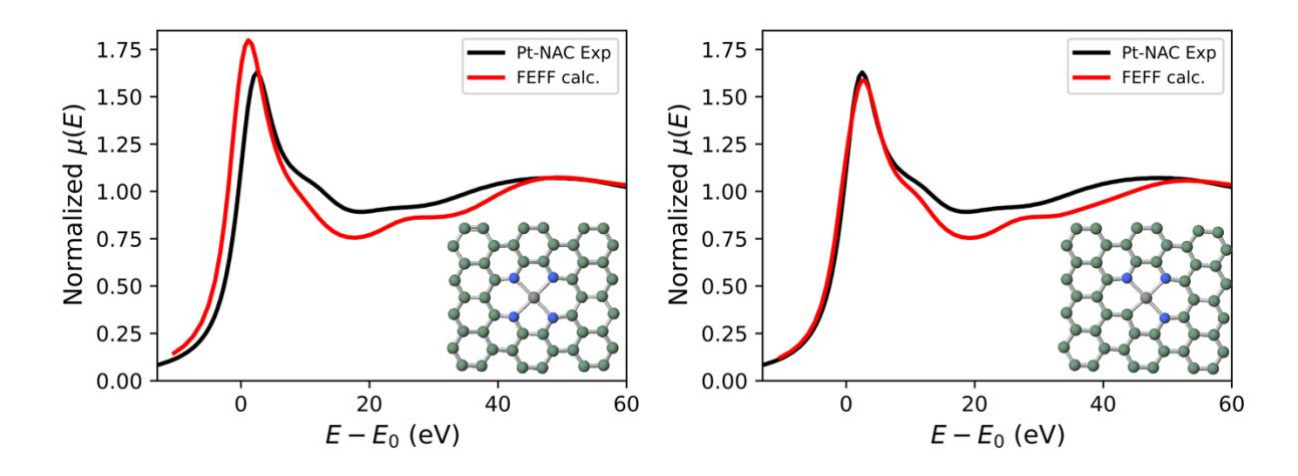


Figure S26. XANES simulation of Pt-NAC.

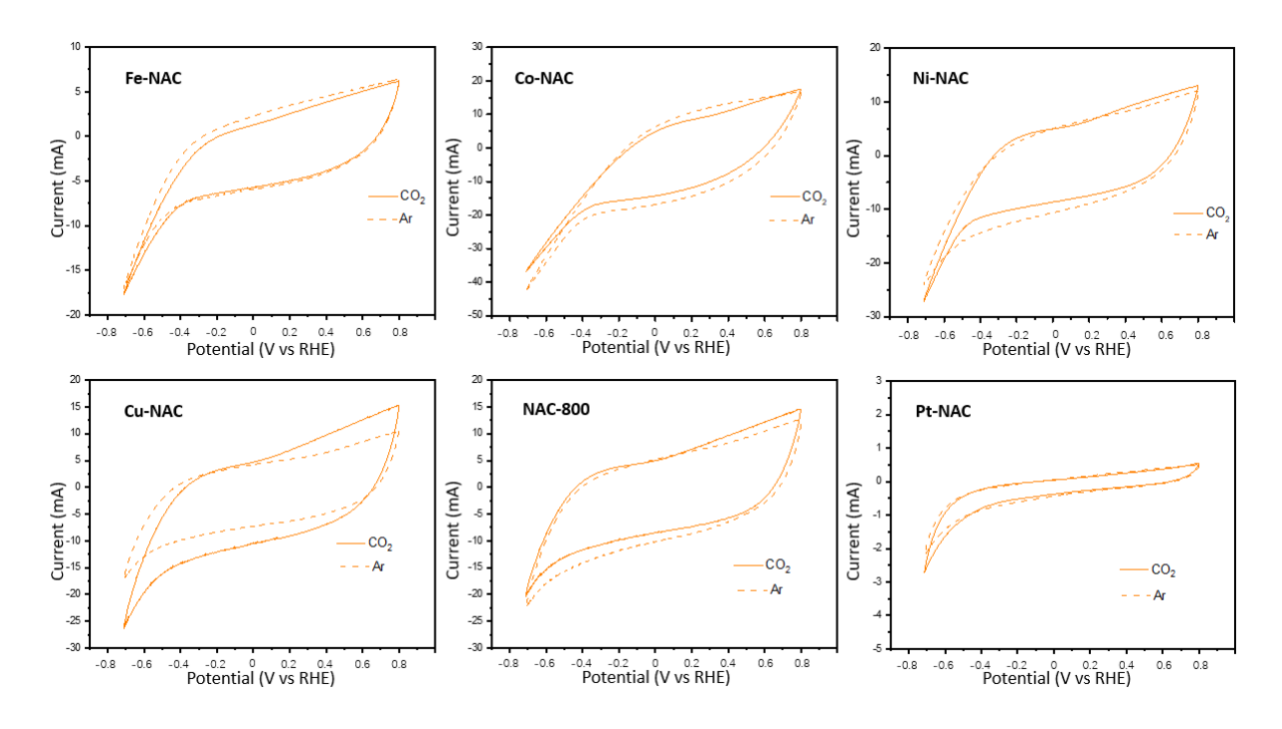


Figure S27. Cyclic voltammetry of different single-atom catalysts in Ar and CO₂ environments.

WILEY-VCH

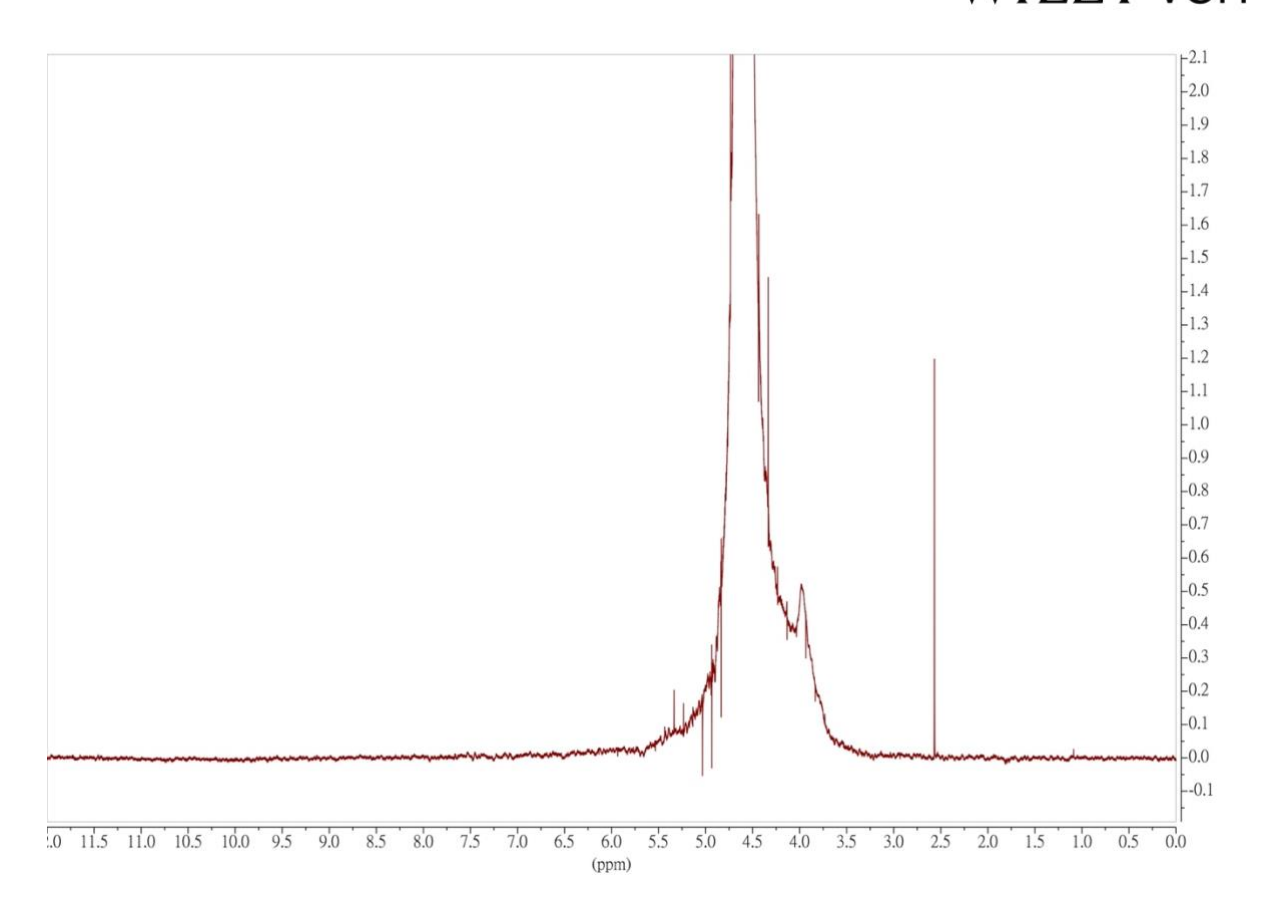


Figure S28. ¹H NMR spectrum for CO₂RR liquid product analysis with Ni-NAC as the catalyst.

WILEY-VCH

Table S4. Recent reported Ni single atom catalysts for electrochemical CO₂ reduction reaction.

Ni catalysts	Atom	Products	Potential	Faradaic	Current	Stability
1 (1 cataly sts	ratio	11044015	(V vs	efficiency	density	(h)
	(%)		RHE)	(%)	(mA cm-2)	
This work	1.7	CO	- 0.8 ~ - 1.4	> 90	151	14
Ni-N-Gr ^[1]	2.2	CO	-0.7	> 90	(-1.4 V) < 0.4	5
Ni-N4 ^[2]	1.41	CO	-0.81	99	28.6	30
N-doped graphene ^[3]	0.8	СО	-0.68	92	30	20
Ni(i)-N4 ^[4]	0.82	CO	-0.5	97	22	100
Unsaturated Ni-N ^[5]	5.44	CO	-0.63	98	71.5	12
Ni single atom ^[6]	0.44	CO	-0.65	95	50	20
Ni-N3-V ^[7]		CO	-0.9	90	65	14
Ni-N ^[8]	2.6	CO	-0.8	90.2	5	6
Ni SA ^[9]	0.28	CO	-1.0	97	49	24
SA Ni decorated carbon ^[10]	1.3	СО	-1.0	88	308	120

WILEY-VCH

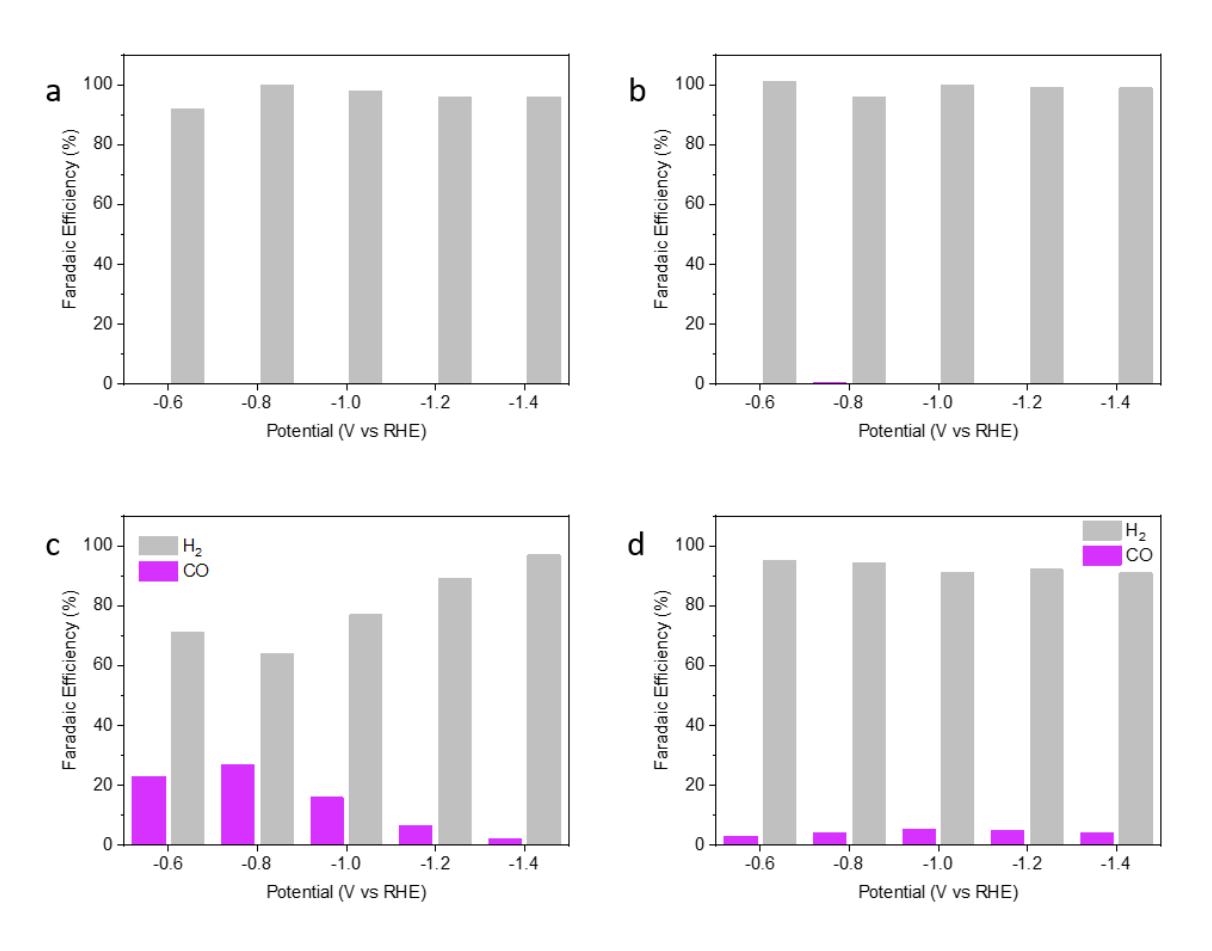


Figure S29. Products distribution of CO₂RR catalyzed by (a) Pt-NAC (b) Ru-NAC (c) Pd-NAC (d) Rh-NAC catalyst at different reduction potentials.

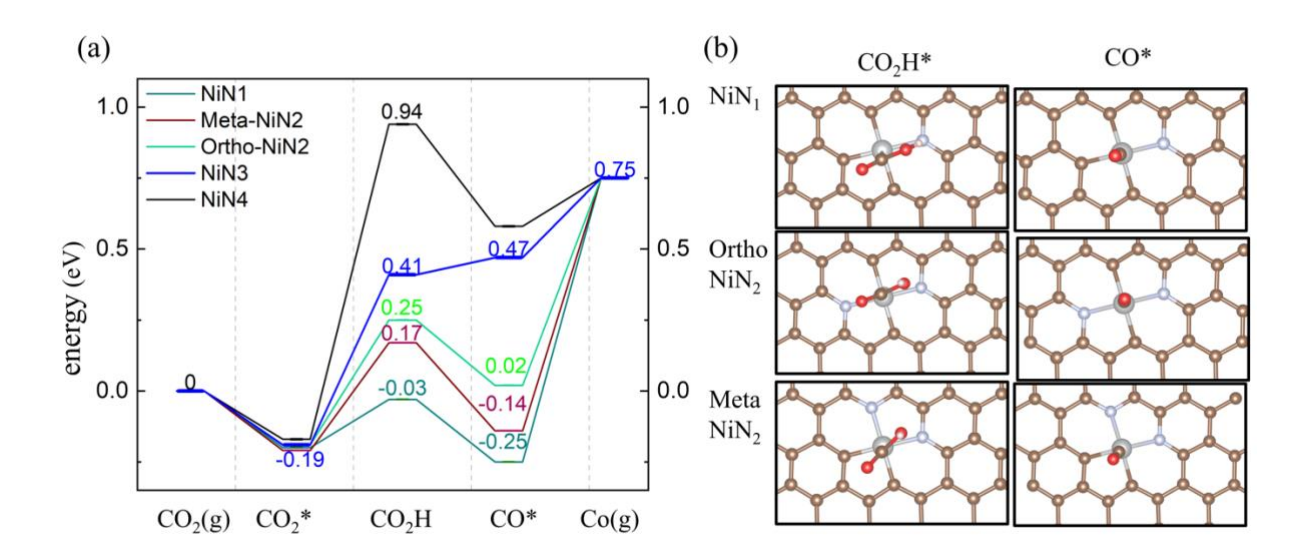


Figure S30. (a) Total energy diagram of CO_2RR on nitrogen-doped graphene with Ni single atoms (NiN_x). N_x indicates the number of N atoms bonding with Ni. (b) The calculated atomic structures of CO_2H and CO on NiN₁ and NiN₂ structures. Over NiN₃ and NiN₄ the reaction is limited by the first protonation step, while on NiN₁ and NiN₂, the rate is limited by CO desorption.

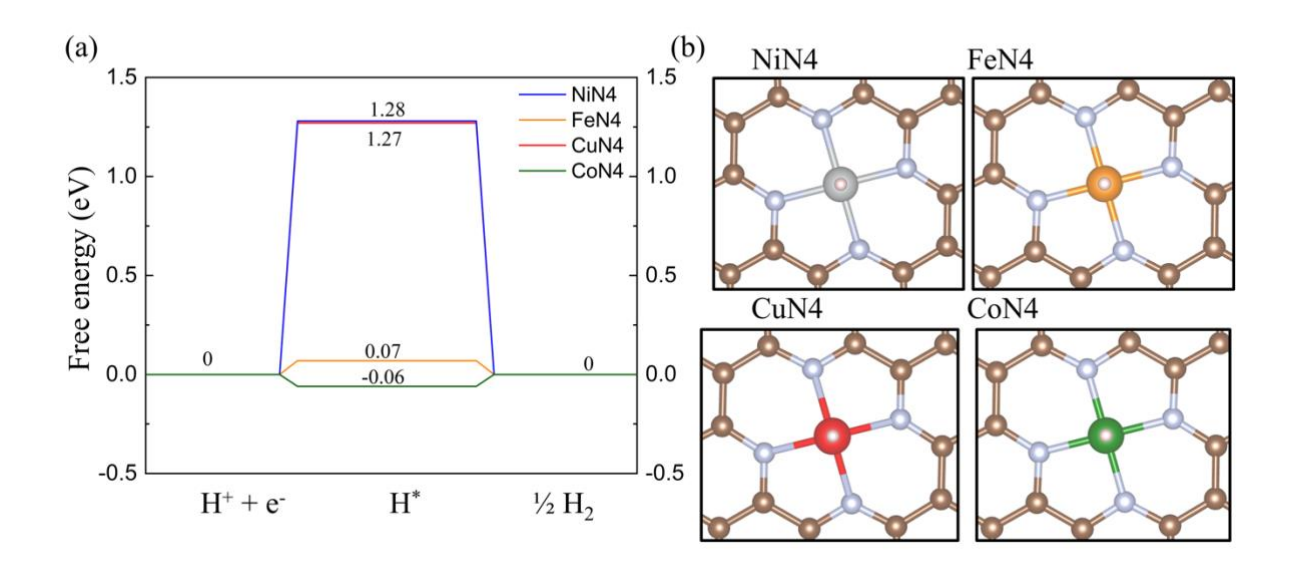


Figure S31. (a) Free energy diagram of HER on N₄-doped graphene single-atom catalyst with single atom Ni, Fe Cu and Co. (b) The calculated structures of H* on each single atom catalyst. The results suggest Ni in N₄ configuration is resistant to HER and have high selectivity toward CO product.

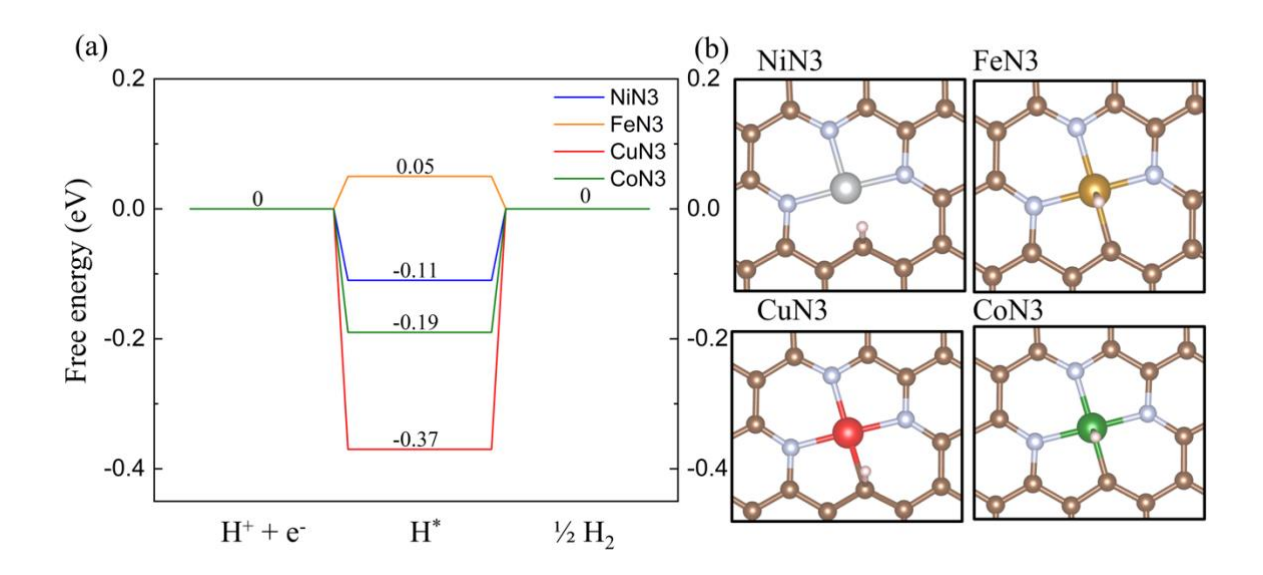


Figure S32. (a) Free energy diagram of HER on N₃-doped graphene single-atom catalysts with single atom Ni, Fe Cu and Co. (b) The calculated structures of H* on each single atom catalyst.

Supporting References:

- [1] Su, P., Iwase, K., Nakanishi, S., Hashimoto, K. and Kamiya, K., 2016. Nickel-nitrogen-modified graphene: an efficient electrocatalyst for the reduction of carbon dioxide to carbon monoxide. *Small*, *12*(44), pp.6083-6089.
- [2] Li, X., Bi, W., Chen, M., Sun, Y., Ju, H., Yan, W., Zhu, J., Wu, X., Chu, W., Wu, C. and Xie, Y., 2017. Exclusive Ni–N4 sites realize near-unity CO selectivity for electrochemical CO2 reduction. *Journal of the American Chemical Society*, *139*(42), pp.14889-14892.
- [3] Bi, W., Li, X., You, R., Chen, M., Yuan, R., Huang, W., Wu, X., Chu, W., Wu, C. and Xie, Y., 2018. Surface immobilization of transition metal ions on nitrogen-doped graphene realizing high-efficient and selective CO2 reduction. *Advanced Materials*, 30(18), p.1706617.
- [4] Yang, H.B., Hung, S.F., Liu, S., Yuan, K., Miao, S., Zhang, L., Huang, X., Wang, H.Y., Cai, W., Chen, R. and Gao, J., 2018. Atomically dispersed Ni (I) as the active site for electrochemical CO 2 reduction. *Nature energy*, *3*(2), pp.140-147.
- [5] Yan, C., Li, H., Ye, Y., Wu, H., Cai, F., Si, R., Xiao, J., Miao, S., Xie, S., Yang, F. and Li, Y., 2018. Coordinatively unsaturated nickel–nitrogen sites towards selective and high-rate CO 2 electroreduction. *Energy & Environmental Science*, 11(5), pp.1204-1210.
- [6] Jiang, K., Siahrostami, S., Zheng, T., Hu, Y., Hwang, S., Stavitski, E., Peng, Y., Dynes, J., Gangisetty, M., Su, D. and Attenkofer, K., 2018. Isolated Ni single atoms in graphene nanosheets for high-performance CO 2 reduction. *Energy & Environmental Science*, *11*(4), pp.893-903.
- [7] Rong, X., Wang, H.J., Lu, X.L., Si, R. and Lu, T.B., 2020. Controlled Synthesis of a Vacancy-Defect Single-Atom Catalyst for Boosting CO2 Electroreduction. *Angewandte Chemie*, *132*(5), pp.1977-1981.
- [8] Mou, K., Chen, Z., Zhang, X., Jiao, M., Zhang, X., Ge, X., Zhang, W. and Liu, L., 2019. Highly Efficient Electroreduction of CO2 on Nickel Single-Atom Catalysts: Atom Trapping and Nitrogen Anchoring. *Small*, *15*(49), p.1903668.
- [9] Zheng, T., Jiang, K., Ta, N., Hu, Y., Zeng, J., Liu, J. and Wang, H., 2019. Large-scale and highly selective CO2 electrocatalytic reduction on nickel single-atom catalyst. *Joule*, *3*(1), pp.265-278.
- [10] Yang, H., Lin, Q., Zhang, C., Yu, X., Cheng, Z., Li, G., Hu, Q., Ren, X., Zhang, Q., Liu, J. and He, C., 2020. Carbon dioxide electroreduction on single-atom nickel decorated carbon membranes with industry compatible current densities. *Nature communications*, 11(1), pp.1-8.